

Large Magnetic Anisotropy in Mono- and Binuclear cobalt(II) Complexes: The Role of the Distortion of the Coordination Sphere in Validity of the Spin-Hamiltonian Formalism

Katarzyna Choroba, Joanna Palion-Gazda, Barbara Machura,* Alina Bienko,* Daria Wojtala, Dariusz Bienko, Cyril Rajnák, Roman Boča, Andrew Ozarowski, and Mykhaylo Ozerov



Cite This: *Inorg. Chem.* 2024, 63, 1068–1082



Read Online

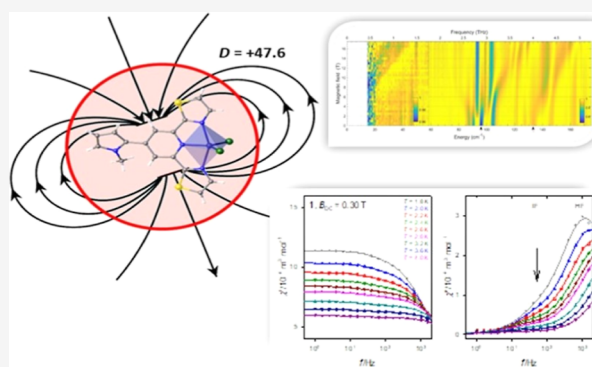
ACCESS |

Metrics & More

Article Recommendations

Supporting Information

ABSTRACT: To get a better insight into understanding the factors affecting the enhancement of the magnetic anisotropy in single molecule (single ion) magnets, two cobalt(II) complexes based on a tridentate ligand 2,6-di(thiazol-2-yl)pyridine substituted at the 4-position with *N*-methyl-pyrrol-2-yl have been synthesized and studied by X-ray crystallography, AC and DC magnetic data, FIRMS and HFEP spectra, and theoretical calculations. The change of the counteranion in starting Co(II) salts results in the formation of pentacoordinated mononuclear [Co(mpyr-dtpy)Cl₂]·2MeCN (**1**) complex and binuclear [Co(mpyr-dtpy)₂][Co(NCS)₄] (**2**) compound. The observed marked distortion of trigonal bipyramid geometry in **1** and cationic octahedral and anionic tetrahedral units in **2** brings up a question about the validity of the spin-Hamiltonian formalism and the possibility of determining the value and sign of the zero-field splitting *D* parameter. Both complexes exhibit field-induced slow magnetic relaxation with two or three relaxation channels at *B*_{DC} = 0.3 T. The high-frequency relaxation time in the reciprocal form $\tau(\text{HF})^{-1} = CT^n$ develops according to the Raman relaxation mechanism (for **2**, *n* = 8.8) and the phonon-bottleneck-like mechanism (for **1**, *n* = 2.3). The high-frequency relaxation time at *T* = 2.0 K and *B*_{DC} = 0.30 T is $\tau(\text{HF}) = 96$ and $47 \mu\text{s}$ for **1** and **2**, respectively.



INTRODUCTION

Slow magnetic relaxation (SMR), as a prerequisite of the single-ion or single-molecule magnet (SIM or SMM), is a rather common feature identified for a lot of the Co(II) complexes. Some of them display SIM properties in the absence of the magnetic field; however, the majority of them are field-supported SIMs with single, two, or three modes of relaxation.^{1–11} This phenomenon was observed in numerous coordination geometries and coordination numbers such as two, three, four, five, six, seven, and eight (Tables S1 and S2, Supporting Information).^{12–35}

Even though a remarkable number of Co(II)-based SIMs have been reported so far, their effective energy barriers for spin reversal usually range from 20 to 50 K. For this reason, great efforts have been made toward finding a solid conceptual explanation of this fact. A paradigm is generally accepted that the relaxation time τ is dominated by the high barrier to spin reversal U_{eff} (referring to the over-barrier Orbach relaxation process) that is proportional to the absolute value of the axial zero-field splitting (zfs) parameter *D* (negative for easy-axis anisotropy or positive for easy-plane anisotropy) and the square of the molecular spin *S*: $U_{\text{eff}} = |D|S^2$ and $U_{\text{eff}} = |D|(S^2 - 1/4)$ for non-Kramers and Kramers ions, respectively. One of the directions is understanding the existence of the zfs and

associated magnetic anisotropy. In principle, the magnetic anisotropy can be controlled through the coordination number and fine-tuned by ligand field strength, counterions, or solvent molecules, which determine the overall molecular structure.^{15–20}

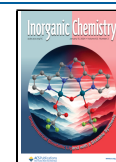
Tetracoordinate (nearly tetrahedral) and hexacoordinate (nearly octahedral) cobalt(II) complexes possess a different degree of magnetic anisotropy, measured primarily by the axial zfs parameter *D* and by the rhombic zfs parameter *E*, when the spin-Hamiltonian (SH) formalism is applicable. For tetracoordinate systems, $|D|$ is typically below 30 cm^{-1} , with rare exceptions, such as the mononuclear tetrahedral cobalt(II) complex $(\text{HNET}_3)_2[\text{Co}^{\text{II}}(\text{L}^{2-})_2]$, where $\text{H}_2\text{L} = 1,2\text{-bis}(\text{methanesulfonamido})\text{benzene}$ with $D = -115 \pm 20 \text{ cm}^{-1}$.²¹ For such systems, *D* is negative for the geometry of a compressed (flattened) bisphenoid toward a square and

Received: September 29, 2023

Revised: December 14, 2023

Accepted: December 19, 2023

Published: January 2, 2024



positive in the opposite distortion. One of the theories directly correlates the δ structural parameter defined for $[\text{CoX}_2\text{Y}_2]$ complexes by two angles, $\angle(\text{X}-\text{Co}-\text{X})$ (α) and $\angle(\text{Y}-\text{Co}-\text{Y})$ (β) $\delta = 2\alpha T_d - (\alpha + \beta)$, where $\alpha T_d = 109.5^\circ$ with D ,²² while another one suggests that such a relationship between δ and D is not linear in general.²³ It has also been shown that heavier and softer terminal ligands are able to significantly modify the anisotropy of Co(II) centers.^{5,24} The breakthrough work of this area was an example of a homoleptic mononuclear compound $(\text{PPh}_4)_2[\text{Co}(\text{SPh})_4]$, which possesses a large negative zfs parameter $D = -70 \text{ cm}^{-1}$ (another exception) and exhibits SIM behavior in a zero static magnetic field.⁵

High positive values of D over the range of 40–120 cm^{-1} were reported for hexacoordinate Co(II) complexes distorted toward a compressed tetragonal bipyramid; these possess the orbitally nondegenerate electronic ground term $^4A_{1g}$, for which the SH formalism is fully applicable, and the zfs can be parameterized by parameters $\{D, E, g_x, g_y, \text{ and } g_z\}$. However, in the case of the hexacoordinate Co(II) systems with the geometry of an elongated tetragonal bipyramid,^{25,26} the ground electronic terms are orbitally doubly degenerate E_g . This case can be treated using the Griffith–Figgis (GF) theory, where parameters such as Δ_{ax} (term splitting), ξ (spin–orbit coupling constant), κ (orbital reduction factor), and A (coefficient of configuration interaction) occur and the D parameter is undefined. This also occurs in some pentacoordinate Co(II) complexes.⁹ It was also found that the axial component of the zfs decreases with large structural distortions, while the in-plane anisotropy increases, leading to lower energy barriers for spin reversal (see Table S1, Supporting Information).

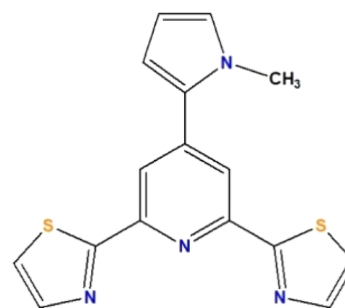
A more complicated situation can be found in the pentacoordinate complexes, which can usually take geometries ranging from trigonal bipyramidal (TBY) to square pyramidal (SPY) with a large contribution of the angular orbital momentum to the ground state. For such systems, the relationship between the geometry of the coordination polyhedron and the magnetic anisotropy is based on the Addison parameter τ . The SPY Co(II) complexes with $\tau < 0.3$ adopt large and negative D values, while for geometries closer to the TBY arrangement, $\tau \approx 1$, the sign of D is changed to positive. Another correlation was later reported for complexes close to a TBY arrangement, for which small values of $|D|$ are expected.²⁷

Relative to the abundant research for SPY and TBY geometry, however, factors affecting the magnetic anisotropy in pentacoordinate Co(II) complexes with coordination geometries intermediate between SPY and TBY are noticeably less studied.^{13,28}

Along this line, to get a better insight into understanding the factors affecting the magnetic anisotropy and dynamics of relaxation processes in Co(II)-based single-ion magnets, we selected 2,6-di(thiazol-2-yl)pyridine substituted at the 4-position with *N*-methyl-pyrrol-2-yl (Scheme 1) to obtain both mono- and binuclear cobalt(II) complexes. In analogy to 2,2':6',2''-terpyridines, this rigid heterocyclic ligand meets the requirement to coordinate to the Co(II) ion by three nitrogen atoms, and the steric hindrance of the methyl group is expected to prevent strong π – π intermolecular interactions in the crystal lattice causing fast quantum tunneling effects.^{36–41}

To our best knowledge, only one cobalt(II) complex with the 4-substituted 2,6-di(thiazol-2-yl)pyridine-based ligand, namely, $[\text{CoL}_2]\text{PF}_6$, where L is 4-(2,2'-bithiophene-5-yl)-2,6-di(thiazol-2-yl)pyridine, has been structurally characterized so

Scheme 1. Ligand 4-(*N*-Methyl-pyrrol-2-yl)-2,6-di(thiazol-2-yl)pyridine (*mpyr-dtpy*)



far, and its preliminary magnetic studies have revealed the high-spin state of the Co(II) center over the temperature range of 10–300 K.⁴¹ Using our previous experience,^{9,34} we synthesized the pentacoordinate mononuclear complex $[\text{Co}(\text{mpyr-dtpy})\text{Cl}_2] \cdot 2\text{MeCN}$ (**1**) and the binuclear one with octahedral-tetrahedral Co(II) units $[\text{Co}(\text{mpyr-dtpy})_2][\text{Co}(\text{NCS})_4]$ (**2**). The detailed magnetochemical and HFEPFPR investigations for these systems confirmed the effectiveness of the 4-(*N*-methyl-pyrrol-2-yl)-2,6-di(thiazol-2-yl)pyridine (*mpyr-dtpy*) multicoordinate ligand in the construction of SMM or SIM materials.

EXPERIMENTAL SECTION

Synthetic Procedures. The air-stable cobalt(II) complexes $[\text{Co}(\text{mpyr-dtpy})\text{Cl}_2] \cdot 2\text{MeCN}$ (**1**) and $[\text{Co}(\text{mpyr-dtpy})_2][\text{Co}(\text{NCS})_4]$ (**2**) were obtained as dark green crystals after heating a solution of 4-(*N*-methyl-pyrrol-2-yl)-2,6-di(thiazol-2-yl)pyridine (*mpyr-dtpy*) with CoCl_2 (for **1**) and $\text{Co}(\text{SCN})_2$ (for **2**) in a mixture of $\text{CHCl}_3/\text{CH}_3\text{CN}$. Details of synthesis and analysis are described in Supporting Information.

Physical Techniques. HR-APCI-MS was performed on a Maxis Impact Bruker mass spectrometer equipped with a Q-TOF-type mass analyzer. The analyzed samples were dissolved in CH_3CN . Full-scan MS data were collected from 50 to 2200 m/z in positive ion mode, and the data were calibrated using the APCI Low Concentration Tuning Mix (Agilent). The recorded data were processed using Data Analysis 4.1 software (Figure S1, Supporting Information). IR spectra were recorded on a Nicolet iS5 FT-IR spectrophotometer in the spectral range 4000–400 cm^{-1} with the samples in the form of KBr pellets (Figure S2, Supporting Information). The electronic spectra were obtained from solid-state samples using Nicolet Evolution 220 (190–1100 nm) and Nicolet iS50 FT-IR (700–1500 nm) spectrophotometers (Figure S4, Supporting Information).

Crystal Structure Determination and Refinement. Powder X-ray diffraction (XRPD) measurements on **1** and **2** were performed on a PANalytical *Empyrean* X-ray diffractometer by using $\text{Cu-K}\alpha$ radiation ($\lambda = 1.5418 \text{ \AA}$), in which the X-ray tube was operated at 40 kV and 30 mA ranging from 5 to 50° (Figure S3, Supporting Information). Experimental patterns measured for polycrystalline samples **1** and **2** are in good agreement with the Mercury 2.4⁴² simulated patterns from the single-crystal X-ray data, demonstrating that the crystal structures are representative of the bulk materials.

Single-crystal X-ray diffraction data were collected on a Gemini A Ultra diffractometer equipped with an Atlas CCD detector and graphite monochromated $\text{MoK}\alpha$ radiation ($\lambda = 0.71073 \text{ \AA}$) at 295 K for **1** and at 295 and 115 K for **2**. Diffraction data collection, unit cell determination, and data reduction were performed using the *CrysAlis Pro* software.^{43,44} The structures were solved by the direct methods using SHELXS and refined by full-matrix least-squares on F^2 using SHELXL-2014.^{45,46} All non-hydrogen atoms were refined anisotropically, while the hydrogen atoms were placed in calculated positions and refined with idealized geometries (riding model) and assigned fixed isotropic displacement parameters: $d(\text{C}-\text{H}) = 0.93 \text{ \AA}$,

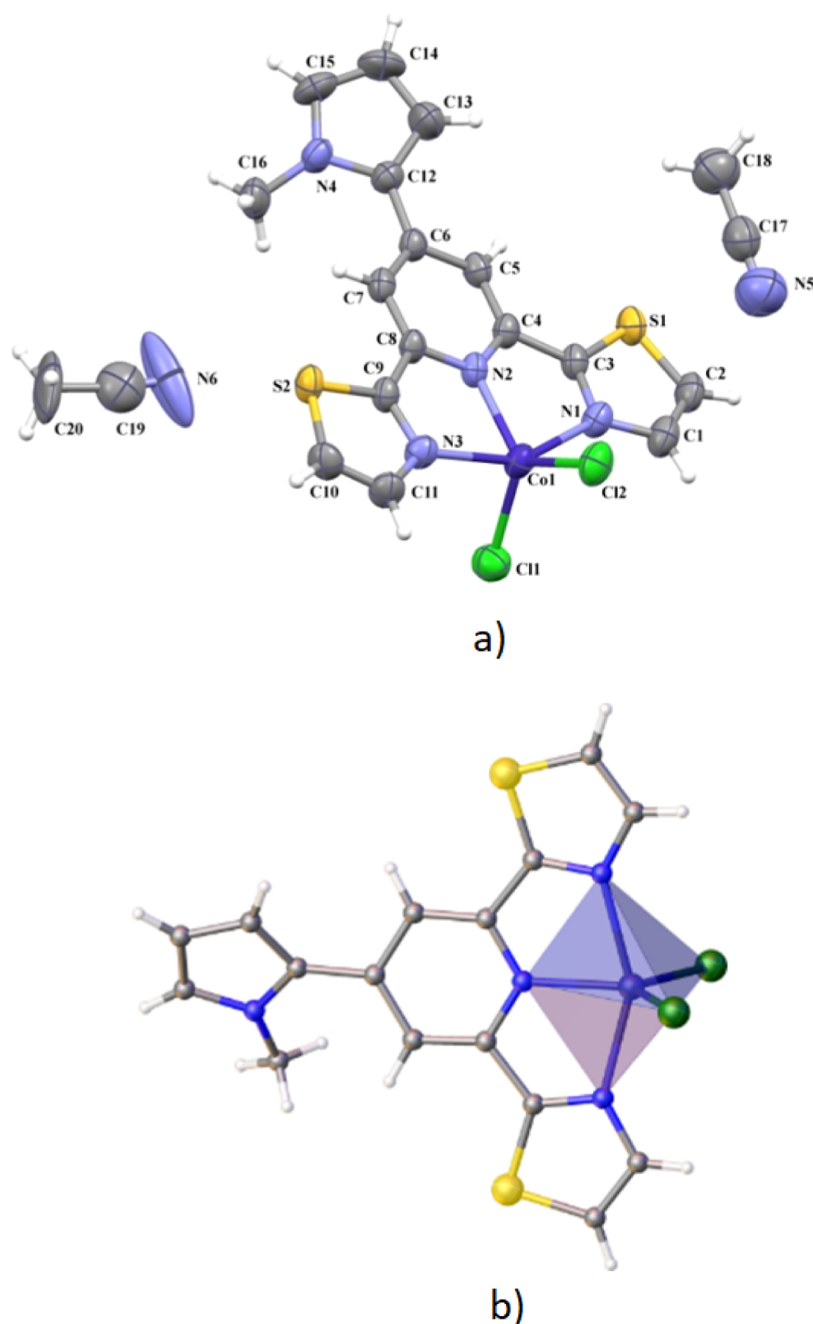


Figure 1. (a) Perspective view of the asymmetric unit of **1** with the atom numbering. The thermal ellipsoids are drawn at the 50% probability level. (b) TBV geometry of the coordination center in $[\text{Co}(\text{mpyr-dtpy})\text{Cl}_2]$.

$U_{\text{iso}}(\text{H}) = 1.2 U_{\text{eq}}(\text{C})$ (for aromatic) and $d(\text{C}-\text{H}) = 0.96 \text{ \AA}$, $U_{\text{iso}}(\text{H}) = 1.5 U_{\text{eq}}(\text{C})$ (for methyl). The methyl groups were allowed to rotate about their local 3-fold axis.

The crystal structures have been deposited at the Cambridge Crystallographic Data Centre with deposition numbers CCDC 2260567 for **1**, 2260568 for **2:295K**, and 2260569 for **2:115K**. Copies of this information may be obtained free of charge from the Director, CCDC, 12 Union Road, Cambridge CB2 1EZ, UK (fax: +44 1223 336033; e-mail: deposit@ccdc.cam.ac.uk or www.ccdc.cam.ac.uk).

HF-EPR and Far-Infrared Magnetic Spectroscopy Studies.

Far-infrared magnetic spectroscopy (FIRMS) was performed at the National High Magnetic Field Laboratory on a 17 T vertical-bore superconducting magnet coupled with a Fourier-transform infrared spectrometer Bruker Vertex 80v. The experimental setup was equipped with a mercury lamp and a composite silicon bolometer

(Infrared Laboratories) as a THz radiation source and detector, respectively. The THz radiation was guided inside an evacuated (~ 4 mbar) optical beamline to the top of the lightpipe probe holding the sample, which is an eicosane pellet containing ~ 4 mg of the studied compound. The intensity of the transmitted THz radiation was measured in the spectral region between 18 and 730 cm^{-1} ($0.55\text{--}22$ THz) with a resolution of 0.3 cm^{-1} (9 GHz). Both the sample and bolometer were cooled by a low-pressure helium gas to a temperature of 5 K. High-frequency EPR spectra were recorded on the 17 T transmission instrument of the EMR facility. The instrument is equipped with a superconducting magnet (Oxford Instruments) capable of reaching a field of 17 T. Microwave frequencies over the range 52–630 GHz were generated by a phase-locked Virginia Diodes source, producing a base frequency of 8–20 GHz, which was multiplied by a cascade of frequency multipliers. The instrument is a transmission-type device and uses no resonance cavity.⁴⁷ The high-

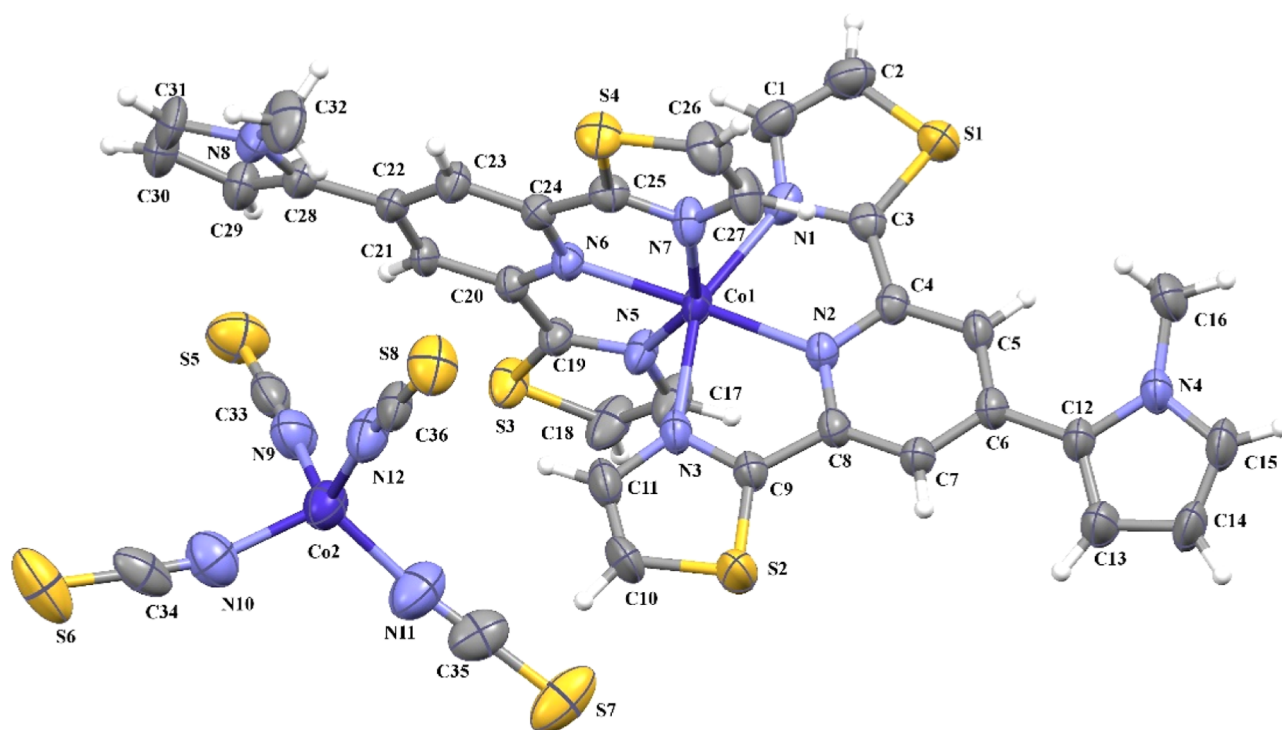


Figure 2. Perspective view of the asymmetric unit of **2**. The thermal ellipsoids of non-hydrogen atoms are drawn at the 50% probability level.

field EPR spectra were simulated using computer programs written by one of us.⁴⁸

Magnetic Data. The DC magnetic data were taken using the SQUID magnetometer (MPMS, Quantum Design) with *ca.* 21 (**1**) or 18 (**2**) mg of sample. The susceptibility data were acquired at $B_{DC} = 0.5$ T between $T = 1.8$ and 300 K. This was corrected to the underlying diamagnetism and transformed to the effective magnetic moment. The magnetization data were taken at low temperatures $T = 2.0$ up to $B = 5.0$ T. No remnant magnetization has been detected. The AC susceptibility data were taken with the same apparatus and the same samples using the oscillating field amplitude $B_{AC} = 0.3$ mT. Three regimes were used: (i) a scan of the AC susceptibility as a function of the field up to $B_{DC} = 1$ T at $T = 2.0$ K for a set of four trial frequencies f ; (ii) a scan of the AC susceptibility as a function of temperature for 22 frequencies of the oscillating field; and (iii) a set of temperatures ranging between $T = 1.8$ and 7.0 (8.0) K, all performed at the properly selected field $B_{DC} = 0.3$ T for complexes **1** and **2**. The magnetic data were analyzed by our own software.⁴⁹

The *ab initio* calculations were performed with the help of the ORCA package in experimental geometries of complexes.^{50–52} ZORA-def2-SV(P)/TZVPP basis sets were used. The CASSCF calculations involved 7 valence electrons in 5 orbitals (10 spin-orbitals), yielding the active space covered by 120 kets. The NEVPT2 module was used in order to improve the transition energies. The spin-orbit coupling was considered in the SOMF approximation. Finally, the effective Hamiltonian theory allowed extracting the D -tensor and g -tensor components, from which the traditional SH parameters $\{D, E, g_x, g_y, \text{ and } g_z\}$ were determined.⁵³

RESULTS AND DISCUSSION

Details of the IR (Figure S2A,B, Supporting Information) and UV spectroscopic characterization (Figure S4, Supporting Information) are described in Supporting Information.

Description of the Structures. Details of the crystallographic data collection, structural determination, and refinement of **1** and **2** are given in Table S3 (Supporting Information), whereas the selected bond distances and angles are listed in Tables S4 and S5 (Supporting Information). For

compound **2**, X-ray analysis was carried out at 295 and 115 K. With the temperature increase from 115 to 295 K, only a slight increase in the cell volume (2.28%) was revealed, indicating that no structural phase transition occurs for **2** in the whole temperature range.

The crystal structure of **1** consists of the complex $[\text{Co}(\text{mppy-dtpe})\text{Cl}_2]$ and solvent MeCN molecules, interlinked by weak hydrogen bonds $\text{C-H}\cdots\text{Cl}$, $\pi\cdots\pi$ interactions involving the pyridyl and thiazolyl rings of the *mppy-dtpe* ligands as well as $\text{C-N}\cdots\pi$ interactions between the uncoordinated acetonitrile and thiazolyl rings (see Tables S6–S8, Supporting Information) into zigzag supramolecular chains propagated along b (shown in Figure S5a, Supporting Information). The shortest intermolecular metal–metal distance is 7.164(1) Å ($\text{Co}(1)\cdots\text{Co}(1)^a$, $[(a) = 1 - x, 1 - y, 1 - z]$).

The metal center in structure **1** is coordinated by two chloride ions and three nitrogen donors from a 2,6-di(thiazol-2-yl)pyridine-based ligand (Figure 1).

By analogy to the terpyridine Co(II) complexes,^{54–58} the $\text{Co-N}_{\text{central}}$ bond length [2.054(3) Å] is shorter in relation to those of the outer thiazolyl rings [2.219(4) and 2.216(3) Å]. The *dtpe* framework is approximately planar, with the dihedral angles between the mean planes of the central pyridine and terminal aromatic rings equal to 5.6 and 1.0°, while the *N*-methyl-pyrrolyl unit is inclined at 32.9° to the central pyridine, minimizing inter-ring $\text{H}\cdots\text{H}$ repulsions.

The angular structural index parameter τ ⁵⁹ equals 0.48, indicating that the $\{\text{CoN}_3\text{Cl}_2\}$ chromophore geometry can be described as an intermediate between TBV and SPY. According to the structural analysis performed with the SHAPE program,⁶⁰ the complex $[\text{Co}(\text{mppy-dtpe})\text{Cl}_2]$ most closely resembles TBV, with the agreement factor $S_Q(\text{TBV}) = 2.11$ significantly lower compared to $S_Q(\text{SPY}) = 4.10$.

For the comparison purpose, the Addison parameter of $[\text{CoCl}_2(\text{terpy})]$ is close to 0, consistent with the SPY geometry

Table 1. Results of the *Ab Initio* Calculations for **1**^a

{Co ^{II} N ₃ Cl ₂ }, 1	KD1	KD2	KD3	KD4
spin-orbit multiplets	$\delta_{1,2} = 0$	$\delta_{3,4} = 98$	$\delta_{5,6} = 1756$	$\delta_{5,6} = 2084$
spin composition	$42 \cdot \pm 1/2\rangle + 53 \cdot \pm 3/2\rangle$	$53 \cdot \pm 1/2\rangle + 44 \cdot \pm 3/2\rangle$	$56 \cdot \pm 1/2\rangle + 41 \cdot \pm 3/2\rangle$	$40 \cdot \pm 1/2\rangle + 56 \cdot \pm 3/2\rangle$
projection norm	$N_{1,2} = 0.96$	$N_{3,4} = 0.98$		
transition energy	SH parameters, score $\Sigma = 313$			
⁴ A ₂ '': $\Delta_0 = 0$	$D = 48.8$	$E/D = 0.06$	$g_1 = 1.984$	
⁴ A ₁ ': $\Delta_1 = 1968$	$D_1 = +9.9$	$E_1 = +4.6$	$g_2 = 2.435$	
⁴ A ₂ ': $\Delta_2 = 2710$	$D_2 = +2.9$	$E_2 = -0.3$	$g_3 = 2.502$	
⁴ E _(a) ': $\Delta_3 = 3972$	$D_3 = +18.9$	$E_3 = +0.2$	$g_{iso} = 2.307$	
⁴ E _(b) ': $\Delta_4 = 5005$	$D_4 = +13.2$	$E_4 = -1.5$		

^aExplanation: $|\pm 1/2\rangle$ means a cumulative percentage of the spin contributions in the given spin-orbit multiplet arising from the lowest roots referring to the block of the spin multiplicity $m = 4$ (sum of contributions >1%); Δ_i —transition energies between terms at the NEVPT2 level; δ_i —energies of the spin-orbit multiplets; $D_i(E_i)$ —contributions to the $D(E)$ parameter from the lowest excitations; all energy data in cm⁻¹. ⁴E_(a)' and ⁴E_(b)' are daughter terms of the mother term ⁴E' on symmetry descent.

around the metal center.⁵⁴ Also, the coordination polyhedra of the vast majority of previously reported [CoCl₂(Rⁿ-terpy)] complexes with 2,2':6',2''-terpyridine substituted at the para position of the central pyridine were found to be closer to square-based pyramidal, and exemplarily, $\tau = 0.07$ for the Co(II) complex with 4'-chloro-2,2':6',2''-terpyridine,⁵⁵ $\tau = 0.02$ and 0.23 for [CoCl₂(Rⁿ-terpy)] with 4'-methoxy-2,2':6',2''-terpyridine,⁵⁶ and $\tau = 0.23$ for [CoCl₂(Rⁿ-terpy)] incorporating 4'-{4-[di(2-pyridyl)aminomethyl]phenyl}-2,2':6',2''-terpyridine.⁵⁶ With reference to the findings about related Cu(II) complexes,^{40,61} the coordination geometry around the Co(II) ion in **1** can be rationalized by the attachment of 1-methyl-1H-pyrrol-2-yl at the 4-position of 2,6-di(thiazol-2-yl)pyridine.

The asymmetric unit of **2** contains the complex cation [Co(mpyr-dtpy)₂]²⁺ and the complex anion [Co(NCS)₄]²⁻ (Figure 2).

The cobalt(II) ion of the cation is coordinated by two *mpyr-dtpy* ligands bound to the metal center in a *mer* fashion, equatorially via thiazolyl nitrogens and axially through pyridine nitrogen atoms to form a tetragonally compressed {CoN₆} octahedral symmetry. The tetragonality parameter, defined as the ratio of the mean in-plane distance to the mean out-of-plane distance, is higher than unity, which is expected for an ideal octahedron. The most relevant structural parameters of **2**·295 K and **2**·115 K are given in Table S9 (Supporting Information).

Upon increasing the temperature, the average values of the Co–N bond lengths of **2** remain constant within the experimental error. The angular distortion of the {CoN₆} chromophore from the idealized octahedral geometry is mostly attributed to the geometrical constraints caused by the presence of two fused five-member chelate rings of the *dtpy* framework, and this is largely reflected in the small bite angles N(1)–Co(1)–N(2) [75.90(10)° in **2**·295 K, 76.09(7)° in **2**·115 K] and N(6)–Co(1)–N(7) [75.09(10)° in **2**·295 K, 75.35(7)° in **2**·115 K] and the significant increase of the N(2)–Co(1)–N(5) angle [112.19(10)° at **2**·295 K, 112.74(7)° at **2**·115 K]. The N–Co–N angles for the nitrogen atoms in *trans* arrangement fall in the range 150.47(10)–169.23(11)°, and the dihedral angle between the least-squares planes of the *dtpy* framework of the two *mpyr-dtpy* ligands is 86.40° for **2**·295 K and 87.04° for **2**·115 K. Additional information about the geometric distortion of [Co(mpyr-dtpy)₂]²⁺ was obtained by performing continuous shape measurement (CShM) calculations.^{60,62,63} The calcu-

lated $S_Q(\text{OC-6})$ of 4.67 in **2**·295 K and 4.64 in **2**·115 K are indicative for severe distortion of [Co(mpyr-dtpy)₂]²⁺ from octahedral geometry. Compared to the $S_Q(\text{TPR-6})$ with respect to the trigonal prism geometry, however, they are significantly smaller (Table S9, Supporting Information).

The parameters Σ and Θ for [Co(mpyr-dtpy)₂]²⁺, defined, respectively, as the sum of the deviation from 90° of the 12 *cis* angles of the CoN₆ octahedron and the sum of the 24 unique N–Co–N angles measured on the projection of two triangular faces of the octahedron along their common pseudo-3-fold axis, are significantly larger than those reported for the low-spin state (LS) of the cobalt(II) center 61.10–99.10° for Σ and 185–319° for Θ ,²¹ signaling the high-spin state (HS) of the cobalt(II) center in [Co(mpyr-dtpy)₂]²⁺. Also, the average Co–N bond distances of 2.137 in **2**·295 K and 2.135 in **2**·115 K are consistent with the typical HS cobalt(II) complexes.³⁴

The cobalt(II) ion of the complex anion [Co(NCS)₄]²⁻ displays a distorted tetrahedral coordination environment defined by four nitrogen atoms from four thiocyanate ligands. All the pseudohalide ions are almost linear with the N–C–S angles in the range of 177.6(5)–179.4(2)°. The distortion of the [Co(NCS)₄]²⁻ ion from the ideal tetrahedral geometry, evidenced by the Co–N bond distances [1.934(4)–1.974(2) Å] and N–Co–N bond angles [103.22(8)–114.46(9)°], was also evaluated by using Okuniewski's (τ_4') parameter⁶⁴ and performing CShM calculations.^{60,62,63} The calculated τ_4' and shape values $S(T_d)$ with respect to the tetrahedron were found to be 0.9367 and 0.23 for **2**·295 K and 0.9319 and 0.26 for **2**·115 K, respectively, demonstrating a rather weak distortion of the metal coordination sphere of [Co(NCS)₄]²⁻.

The crystal packing analysis (Mercury 3.10 program)^{42,65} demonstrates that the complex cations [Co(mpyr-dtpy)₂]²⁺ are arranged via C–H⋯ π and π ⋯ π interactions into supramolecular planes (Figure S6a and Tables S7 and S8, Supporting Information), which are further joined by [Co(NCS)₄]²⁻, connecting with the complex cations [Co(mpyr-dtpy)₂]²⁺ through C–H⋯S, C–H⋯N, and C–S⋯ π interactions (Figure S6b and Tables S6 and S8, Supporting Information).

The shortest intermetallic separation in the supramolecular plane formed by the [Co(mpyr-dtpy)₂]²⁺ fragments is 10.4668(9) Å in **2**·295 K and 10.3815(5) Å in **2**·115 K, while the shortest Co⋯Co distances between [Co(mpyr-dtpy)₂]²⁺ and [Co(NCS)₄]²⁻ are 6.4006(7) Å in **2**·295 K and 6.3718(5) Å in **2**·115 K. The [Co(NCS)₄]²⁻ anions are isolated from each other with distances of 10.1713(8) Å in **2**·

295 K and 10.1166(6) Å. It is noteworthy that only minor changes in the intermolecular contacts can be noticed between 2•295 and 2•115 K structures (Figure S7 and Tables S3–S5, Supporting Information).

Ab Initio Calculations. For **1**, the calculated energies of the lowest quartet electronic terms arising from the 4F atomic term at the CASSCF + NEVPT2 level lie at $\{^4A_2'': 0\}$, $\{^4A_1' + ^4A_2': 1968, 2710\}$, $\{^4E': 3972, 5005\}$, and $\{^4E'': 9307, 11,355\}$ cm^{-1} (Table 1).

The assignment of the irreducible representations for the D_{3h} symmetry group is done according to the crystal-field calculations depicted in Figure 3.

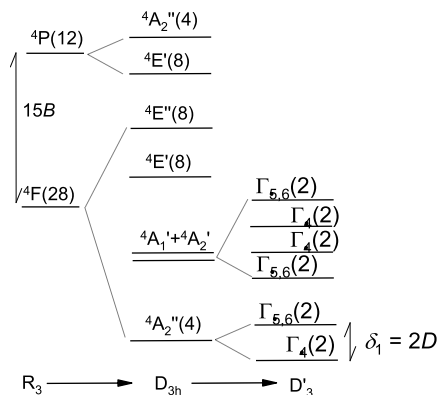


Figure 3. Lowest quartet energy levels for a Co(II) complex with the geometry of TBV (not to scale). Electronic terms are assigned via the Mulliken notation; the multiplets (Kramers doublets) using the Bethe notation in the respective double group $D_{3'}$.

Inclusion of the spin–orbit coupling operator gave a set of spin–orbit multiplets: the lowest 6 Kramers doublets arising from the atomic 4F term lie at $\{\Gamma_4: 0, \Gamma_{5,6}: 98\}$ and $\{\Gamma_{5,6}: 1756, \Gamma_4: 2084, \Gamma_4: 2891, \Gamma_{5,6}: 3065\}$ cm^{-1} . The second KD at $\delta_{3,4} = 98$ cm^{-1} is well separated from the rest of the energy spectrum: $\delta_{5,6} = 1756$ cm^{-1} . (The positions of Kramers doublets are numbered as $\delta_{1,2} = 0, \delta_{3,4}, \delta_{5,6}, \delta_{7,8},$ etc.)

This target space is then projected to a model space of only 4 spin functions $|S, M_S\rangle$ for the fictitious spin $S = 3/2$. The quality of the SH concept can be assessed by the norm of the projected states: when N_I is not far from 1, the projection technique works properly and the SH formalism can be applied. To assess the validity of the SH formalism, the following criterion (score) has been introduced

$$\sum = {}^m\Delta_1 \cdot (\delta_{m+1} - \delta_m) \cdot N_1 / 10,000 \quad (1)$$

where ${}^m\Delta_1$ —first transition energy at the CASSCF + NEVPT2 level; δ_m —energy of the spin–orbit multiplet for the last member of the model space ($m = 4$); δ_{m+1} —first spin–orbit multiplet outside the model space ($m = 5$); and N_1 —projection norm for the first member of the model space. The numerical factor scales the result to a more appropriate size. Such a parameter accounts for the separation of the model space defined by the SH from the rest of the energy spectrum. The value of $\sum = 313 \gg 50$ for **1** indicates that the SH formalism works in the present case.^{66,67} The spin–orbit multiplets can be analyzed in more detail to get their compositions from the pure spin functions $w_1|\pm 1/2\rangle + w_2|\pm 3/2\rangle$ by using the weights calculated from the corresponding transformation matrix.

Having proved the validity of the SH, we can pursue the evaluation of the D -tensor; the axial and rhombic zfs parameters are obtained in a standard way (by diagonalizing the D -tensor and making it traceless, identifying D_{zz} as the diagonal element of the largest absolute value, and using the $E/|D| < 1/3$ constraint). The zfs parameters are $D/hc = 48.8$ cm^{-1} , $E/D = 0.06$, $g\{1.984, 2.435, 2.502\}$, and $g_{\text{iso}} = 2.307$. The D magnitude so obtained is reasonably consistent with the test value for the SH parameters $D_{\text{test}} = \lambda(g_z - g_{xy})/2 = (-515/3)(1.984 - 2.469)/2 = 42$ cm^{-1} ; this is applicable when the direction of g_z coincides with that of D_{zz} .

For the tetracoordinate unit in **2**, the bond lengths Co–N are $d\{1.957, 1.967, 1.967, 1.934\}$ Å and the bond angles N–Co–N are $\theta\{108, 114, 112, 114, 106, 103\}$ deg, showing a marked distortion from the regular tetrahedron. For the tetrahedral unit in **2**, the crystal field of the D_{2d} symmetry splits the 4T_2 and 4T_1 mother terms to $\{^4B_2, ^4E\}$ and $\{^4A_2, ^4E\}$, respectively (Figure 4).

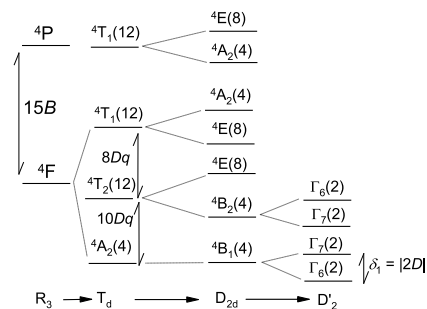


Figure 4. Lowest quartet energy levels for a tetracoordinate Co(II) unit with the geometry of a distorted tetrahedron (prolate bispinoid). Electronic terms are assigned via the Mulliken notation; the multiplets (Kramers doublets) using the Bethe notation in the respective double group $D_{2'}$.

The calculated energies of the lowest quartet daughter terms lie at $\{^4B_1: 0\}$, $\{^4T_2 \rightarrow ^4B_2: 4706; ^4E: 5399, 5855\}$, and $\{^4T_1(F) \rightarrow ^4E: 8861, 9227; ^4A_2: 9466\}$ cm^{-1} (Table 2). The spin–orbit corrected energy levels (6 Kramers doublets) lie at $\{\Gamma_6: 0, \Gamma_7: 8.5\}$, $\{\Gamma_7: 4668, \Gamma_6: 4786\}$, and $\{5339, 5485\}$ cm^{-1} . The projection norm $N_1 = 0.98$ and the score $S = 2149$ confirm the validity of the SH approach.

A subsequent evaluation of the SH parameters gave $D/hc = -3.7$ cm^{-1} , $E/D = 0.32$, $g\{2.204, 2.230, 2.263\}$, and $g_{\text{iso}} = 2.232$. The E/D value is close to the critical point $1/3$ when the sign of D can be reverted, and thus, it is unsure. The energy gap $\delta_{3,4}/hc = 8.5$ cm^{-1} is consistent with the SH parameters $\delta = 2(D^2 + 3E^2)^{1/2}$. The D and g parameters are consistent with the test equation $D_{\text{test}} = -4.0$ cm^{-1} . Note that the D and E values determined from HFEP and FIRMS data are $D = -5.65$ cm^{-1} and $E = -1.86$ cm^{-1} , and the resulting experimental gap is $\delta_{3,4} = 13$ cm^{-1} (see below).

The magnetism of the hexacoordinate unit in **2** is a complex task. The calculated energies of the quartet electronic terms are $\{^4T_{1g} \rightarrow ^4E_g: 0, 413; ^4A_{2g}: 1412\}$, $\{^4T_{2g} \rightarrow ^4B_{2g}: 7521; ^4E_g: 9009, 9136\}$, and $\{^4A_{2g} \rightarrow ^4B_{1g}: 20,052\}$ cm^{-1} . (This spectrum is overlapped with the doublet electronic terms.) The first electronic levels unambiguously show that the ground electronic term of **2b** in the geometry of the elongated tetragonal bipyramid is an orbitally doubly degenerate daughter term 4E_g (Figure 5).

Table 2. Results of the *Ab Initio* Calculations for the Tetracoordinate Unit of 2

[Co ^{II} (NCS) ₄] ²⁻ , 2a	KD1	KD2	KD3	KD4
spin-orbit multiplets	$\delta_{1,2} = 0$	$\delta_{3,4} = 8.5$	$\delta_{5,6} = 4668$	$\delta_{5,6} = 4786$
spin composition	$8\cdot \pm 1/2\rangle + 90\cdot \pm 3/2\rangle$	$90\cdot \pm 1/2\rangle + 8\cdot \pm 3/2\rangle$	$91\cdot \pm 1/2\rangle + 2\cdot \pm 3/2\rangle$	$3\cdot \pm 1/2\rangle + 93\cdot \pm 3/2\rangle$
projection norm	$N_{1,2} = 0.98$	$N_{3,4} = 0.99$		
transition energy ^a	SH parameters, score $\Sigma = 2149$			
⁴ B ₁ : $\Delta_0 = 0$	$D = -3.7$	$E/D = 0.32$	$g_1 = 2.204$	
⁴ B ₂ : $\Delta_1 = 4706$	$D_1 = -24.0$	$E_1 = +0.2$	$g_2 = 2.230$	
⁴ E _(a) : $\Delta_2 = 5399$	$D_2 = +10.8$	$E_2 = -8.9$	$g_3 = 2.263$	
⁴ E _(b) : $\Delta_3 = 5855$	$D_3 = +9.3$	$E_3 = +7.6$	$g_{\text{iso}} = 2.232$	

^a⁴E_{g(a)} and ⁴E_{g(b)} are daughter terms of the mother term ⁴E_g on symmetry descent. Note the high projection norms and high score Σ that justify the SH formalism.

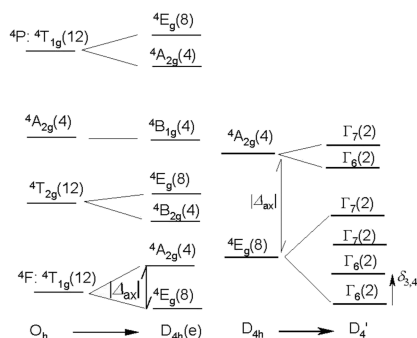


Figure 5. Lowest quartet energy levels for a hexacoordinate Co(II) unit with the geometry of an elongated tetragonal bipyramid. Electronic terms are labeled according to the Mulliken notation, while the ground doublets are labeled using the Bethe notation in the double group D_4' .

The spin-orbit corrected multiplets (6 Kramers doublets) arising from the $4T_{1g} \rightarrow 4E_g + 4A_{2g}$ terms lie at the energies $\{\Gamma_6: 0, \Gamma_6: 187, \Gamma_7: 654, \Gamma_7: 940\}$ and $\{\Gamma_6: 1719, \Gamma_7: 1834\}$ cm^{-1} (Table 3).

The projection norm of the first KD is $N_1 = 0.69$, which is far from the ideal value of 1; small score $S = 13$ indicates a violation of the SH formalism. Therefore, the calculated SH parameters (though its evaluation was activated), including the sign of D , could be false. Note that transitions at 157 and 635 cm^{-1} were observed in FIRMS.

HFEPR and FIRMS. In the HFEPR spectra for 1, three features are observed at the frequency-independent effective g values shown in Figure 6.

This is typical for Co(II) with very large zfs. In such a situation, only transitions within the ground doublet are

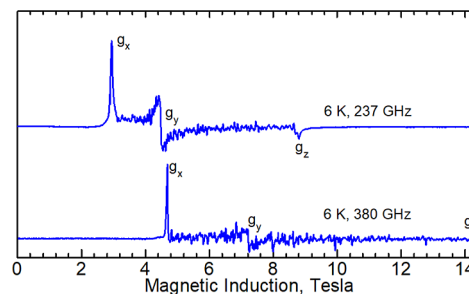


Figure 6. HFEPR spectra of 1 recorded at the conditions shown. The resonances are observed at the effective values $g_x = 5.76$, $g_y = 3.78$, and $g_z = 1.92$. The “false noise” is explained in the text.

observed. The “false noise” seen in these spectra is caused by insufficient sample grinding. Unfortunately, it was found that more thorough grinding caused sample destruction and the appearance of a very different spectrum (see Figure S8, Supporting Information). This may be caused by the compound losing the solvent molecules. Nevertheless, the effective g values could be easily determined for the gently ground species. In FIRMS, a magnetic transition is observed at zero magnetic field, occurring at a frequency around 96 cm^{-1} , with a tolerance of $\pm 5 \text{ cm}^{-1}$, as the spectra are influenced by significant spin-phonon coupling effects (Figure 7).

In the case of 2, three zero-field transitions were observed in the FIRMS spectra (Figure 8): one at about 13 cm^{-1} and the other two at 157 and 632 cm^{-1} .

On the basis of the *ab initio* calculations, we attribute the lower-energy transition to the tetrahedral unit in the structure, while the other ones come from the octahedral molecule, to which the SH formalism cannot be applied. That latter mode is masked by phonon absorption and shows up at a high

Table 3. Results of the *Ab Initio* Calculations for the Hexacoordinate Unit of 2^a

{Co ^{II} N ₆ } ²⁺ , 2b	KD1	KD2	KD3	KD4
spin-orbit multiplets	$\delta_{1,2} = 0$	$\delta_{3,4} = 187$	$\delta_{5,6} = 654$	$\delta_{5,6} = 940$
spin composition	$32\cdot \pm 1/2\rangle + 67\cdot \pm 3/2\rangle$	$66\cdot \pm 1/2\rangle + 31\cdot \pm 3/2\rangle$	$64\cdot \pm 1/2\rangle + 34\cdot \pm 3/2\rangle$	$34\cdot \pm 1/2\rangle + 65\cdot \pm 3/2\rangle$
projection norm	$N_{1,2} = 0.69$	$N_{3,4} = 0.88$		
transition energy	SH parameters, warning: score $\Sigma = 13$			
⁴ E _{g(a)} : $\Delta_0 = 0$	$D = -85.7$	$E/D = 0.26$	$g_1 = 1.934$	
⁴ E _{g(b)} : $\Delta_1 = 413$	$D_1 = -107.6$	$E_1 = -0.001$	$g_2 = 2.191$	
⁴ A _{1g} : $\Delta_2 = 1412$	$D_2 = +16.6$	$E_2 = -16.7$	$g_3 = 2.993$	
⁴ B _{2g} : $\Delta_3 = 7521$	$D_3 = +3.6$	$E_3 = -1.0$	$g_{\text{iso}} = 2.373$	
^b ⁴ E _{g(a)} : $\Delta_4 = 9009$	$D_4 = +5.1$	$E_4 = +4.25$		
^b ⁴ E _{g(b)} : $\Delta_5 = 9136$				

^aNote the low projection norms and low score Σ that challenge the SH formalism.

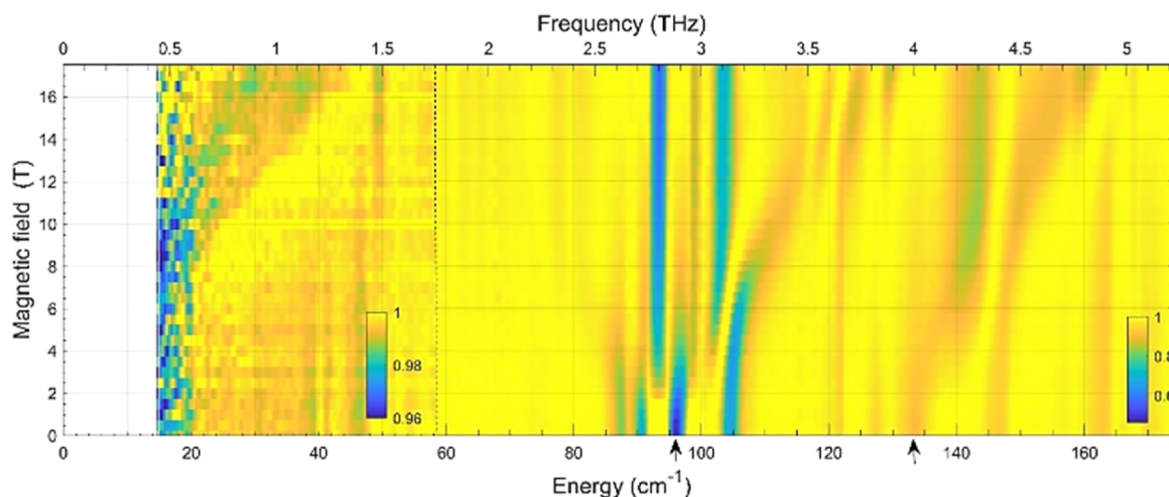


Figure 7. FIRMS map of complex 1. The color scale maps the relative variation of the far-IR transmission spectra with yellow indicating an area insensitive to the magnetic field and blue representing the intensity of the magnetic resonance absorption. The complex pattern with multiple absorption lines at about 87, 91, 105, 121, 146, and 163 cm^{-1} is due to spin-phonon couplings, leading to the small shift of the nominally nonmagnetic phonon absorptions. The zfs value of $2D' = 96(5)$ and the second magnetic absorption at 133(1) cm^{-1} are shown with a black arrow. The color scale below 58 cm^{-1} is different to emphasize the low-frequency branches of magnetic resonance absorption, which were also observed by HF-EPR measurements (Figure 6). White gaps below 14 cm^{-1} show the area below the sensitivity level of the FIRMS technique. The raw far-IR transmission spectra are shown in Figure S9, Supporting Information.

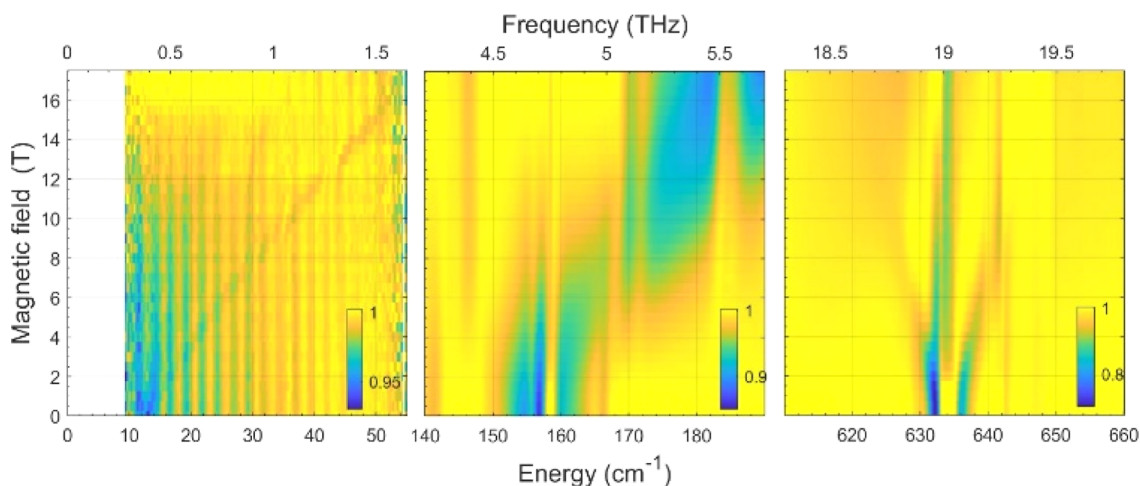


Figure 8. FIRMS map of complex 2. The color scale represents the relative variation of the far-IR transmission spectra induced by the applied magnetic field, similar to Figure 7. The zero-field energy differences between magnetic multiplet states are estimated as 12.8(2), 157(1), and 632(1) from left to right plots, respectively. The vertical lines in the left plot are instrumental artifacts. White gaps below 10 cm^{-1} show the area below the sensitivity level of the FIRMS technique. The raw far-IR transmission spectra are shown in Figure S10, Supporting Information.

magnetic field. It might be attributed to the position of the third Kramers doublet $\delta_{5,6}$, whose energy, 654 cm^{-1} , was found from the *ab initio* calculations.

In the HF-EPR spectra for **2**, two sets of resonances are observed, one of which is characteristic for a Co(II) with extremely large zero-field splitting, so that only resonances occurring within the ground doublet $M_S = \pm 1/2$ are seen (Figure 9).

Another set of observed resonances is characteristic for Co(II) with moderate zero-field splitting. A zero-field transition was observed at 390 GHz, corresponding to 13 cm^{-1} in good agreement with the FIRMS data. The resonances due to the tetrahedral unit were selected, plotted against the microwave frequency, and fitted to determine the SH parameters (Figure 10).

The fitted SH parameters are $g_x = 2.200(1)$, $g_y = 2.164(3)$, $g_z = 2.282(5)$, $D = -5.65(1) \text{ cm}^{-1}$, $E = -1.86(1) \text{ cm}^{-1}$, and $E/D = 0.329$. Although the ratio E/D is almost equal to 1/3, the sign of D could still be determined because the resonances occurring at the Y and Z orientations are sufficiently split, thanks mainly to g_y being substantially different from g_z (they would collapse into one transition if E/D were exactly equal to 1/3 and $g_z = g_y$). Figure 9 shows that assuming the incorrect (positive) sign of D and E causes the incorrect intensity pattern of the spectral features (green line). For example, the feature in the 506 GHz spectrum (Figure 9), appearing at 6.7 T, is dominated by a Z transition, which is simulated properly with negative D and E . If the parameters were positive, the feature would be dominated by a Y transition at 7.2 T, as seen in the green simulated trace. The resonance fields for these Y and Z transitions do not depend on the sign of D and E , but their

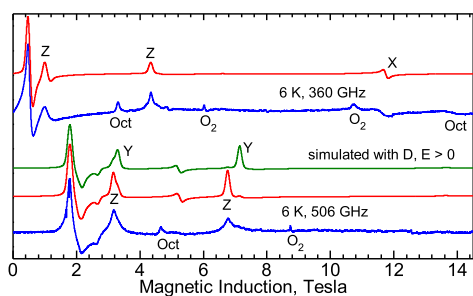


Figure 9. HFEPR spectra of **2**. Blue: experimental; red: simulated with $g_x = 2.200$, $g_y = 2.164$, $g_z = 2.282$, $D = -5.65$ cm^{-1} , and $E = -1.86$ cm^{-1} . The green trace was simulated with $D = +5.65$ cm^{-1} and $E = +1.86$ cm^{-1} to demonstrate the effect of the sign of the zfs parameters. Labels X, Y, and Z indicate the molecular orientations at which respective transitions occur. Signals of molecular oxygen adsorbed on the sample (are marked "O₂", and "Oct" indicates features due to the octahedral unit.

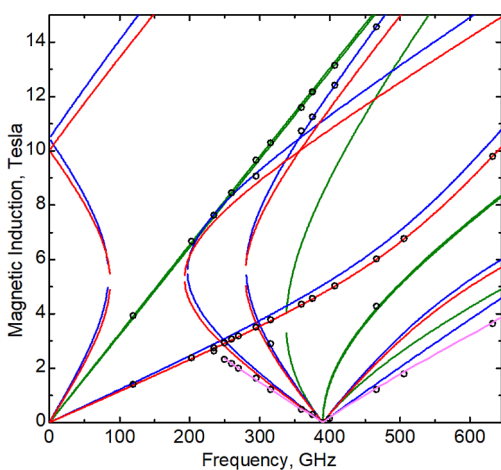


Figure 10. Frequency dependencies of the resonances due to the tetrahedral species in **2**. Open circles are the experimental points. The green, blue, and red lines represent resonances at the molecular X, Y, and Z orientations, respectively, which were calculated using $g_x = 2.200$, $g_y = 2.164$, $g_z = 2.282$, $D = -5.65$ cm^{-1} , and $E = -1.86$ cm^{-1} . The two magenta branches emerging on each side of 390 GHz represent an off-axis turning point. Their calculated positions were read out from the simulated powder spectra.

intensities do depend on the sign. Note that for such considerations, the sign of both D and E must be inverted if g_x is not equal to g_y (see also Supporting Information). The *ab initio* calculations for the insulated $[\text{Co}(\text{NCS})_4]^{2-}$ complex (**2a**) gave $\mathbf{g}\{2.20, 2.23, 2.26\}$, $D = -3.7$ cm^{-1} , and $E/D = 0.32$.

DC Magnetic Data. The DC magnetic data (the temperature dependence of the effective magnetic moment and the field dependence of the magnetization per formula unit) are displayed in Figure 11.

For **1**, the room-temperature effective magnetic moment is $\mu_{\text{eff}} = 5.07$ μ_{B} , which is a typical value for the high-spin mononuclear Co(II) complex with $S = 3/2$ and $g_{\text{av}} = 2.62$. On cooling, it stays almost constant down to 100 K and then gradually decreases to 3.84 μ_{B} at $T = 1.8$ K. This feature is consistent with a sizable zero-field splitting D . Also, the magnetization curve at $T = 2.0$ K does not saturate to a spin-free value of $M_{\text{sat}} \sim g_{\text{av}}S$; this again suggests large zero-field splitting.

SHAPE analysis for complex **1** confirms that the lowest agreement factor $\text{AF} = 2.12$ corresponds to TBPY-5 (D_{3h} , TBY). In such a case, the ground electronic term is the orbitally non-degenerate, $^4A_2''$. Therefore, the SH formalism is applicable. In fitting of the DC magnetic data, the following SH has been used

$$\begin{aligned} \hat{H} &= [\hat{H}_k^{\text{zfs}}] \\ &= D(\hat{S}_z^2 - \bar{S}^2/3)\hbar^{-2} + \mu_{\text{B}}B(g_{xy} \sin \theta_k \hat{S}_x + g_z \cos \theta_k \hat{S}_z) \\ &\quad \hbar^{-1} \end{aligned} \quad (2)$$

In the Zeeman term, 11 orientations of the magnetic field were used to better mimic the powder average. The justification of the SH was obtained by *ab initio* calculations. The fitting procedure converged to the following set of magnetic parameters for **1**: $g_z = 2.0$, $g_{xy} = 2.81$, $D/hc = 47.6$ cm^{-1} , and the molecular-field correction $zj/hc = -0.023$ cm^{-1} ; discrepancy factors of the fit $R(\chi) = 0.023$ and $R(M) = 0.034$. Large anisotropy of the g -factor is a well-known property of the pentacoordinate Co(II) complexes, and it is consistent with the large axial zero-field splitting parameter $D > 0$. The determination of the zero-field splitting E -parameter from the powder data taken above 2 K is an unrealistic task. Therefore, the estimate of the energy gap between the ground and the first crystal-field multiplets is $\delta = 2D = 95$ cm^{-1} , which matches the *ab initio* calculations perfectly and is in good agreement with the 96 cm^{-1} transition observed in FIRMS.

Complex **2**, consisting of two units, behaves differently. The hexacoordinate unit **2a** has a coordination polyhedron with the $\{\text{CoO}_6\}$ chromophore close to an octahedron, where the orbital angular momentum is not quenched. Being close to the $^4T_{1g}$ ground term, the product function χT and/or effective magnetic moment passes through a round maximum. This is evident in Figure 12. Such a maximum cannot be recovered by the SH formalism, which in the high-temperature limit gives a straight line.

The tetra-coordinate unit **2b**, on the contrary, is close to a tetrahedron with the ground electronic term $^4A_{2g}$, in which the orbital angular momentum is absent and, consequently, the SH formalism is justified. This is an unusual situation when two complex units in the same compound require different theoretical explanations. The combined GF + zfs Hamiltonian is

$$\begin{aligned} \hat{H} &= [\hat{H}_k^{\text{GF}}] + [\hat{H}_k^{\text{zfs}}] = [-(A\kappa\lambda)(\vec{L}_p \cdot \vec{S}_1)\hbar^{-2} \\ &\quad + \Delta_{\text{ax}} \left(\hat{L}_{p,z}^2 - \frac{\vec{L}_p^2}{3} \right) \hbar^{-2} \\ &\quad + \mu_{\text{B}}Bg_e(\sin \theta_k \hat{S}_{1x} + \cos \theta_k \hat{S}_{1z})\hbar^{-1} \\ &\quad + \mu_{\text{B}}Bg_L(\sin \theta_k \hat{L}_x + \cos \theta_k \hat{L}_z)\hbar^{-1} \\ &\quad + [D_{\text{Td}}(\hat{S}_{2z}^2 - \bar{S}_2^2/3)\hbar^{-2} + \mu_{\text{B}}Bg_{\text{Td}}(\sin \theta_k \hat{S}_{2x} \\ &\quad + \cos \theta_k \hat{S}_{2z})\hbar^{-1}] \end{aligned} \quad (3)$$

where λ —spin-orbit splitting parameter within the ground term, κ —orbital reduction factor, A —Figgis CI coefficient, Δ_{ax} —axial crystal-field splitting, g_e —free electron magnetogyric factor, and $g_L = -A\kappa \sim -1$. The numerical procedure converged to the following set of magnetic parameters for **2**: $A\kappa\lambda/hc = -119$ cm^{-1} , $g_L = -A\kappa = -1.25$, $\Delta_{\text{ax}}/hc = -1200$

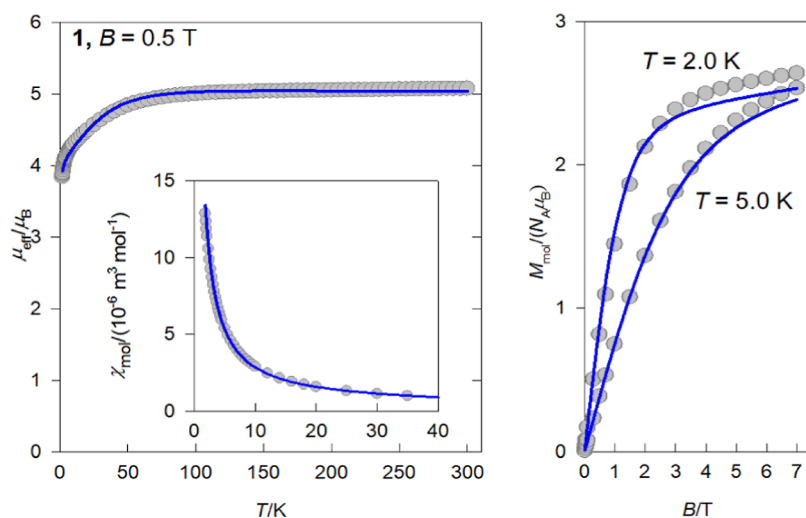


Figure 11. DC magnetic data for 1: left—temperature dependence of the effective magnetic moment (inset: molar magnetic susceptibility in SI units); right—field dependence of the magnetization per formula unit. Solid lines—fitted using SH (see text).

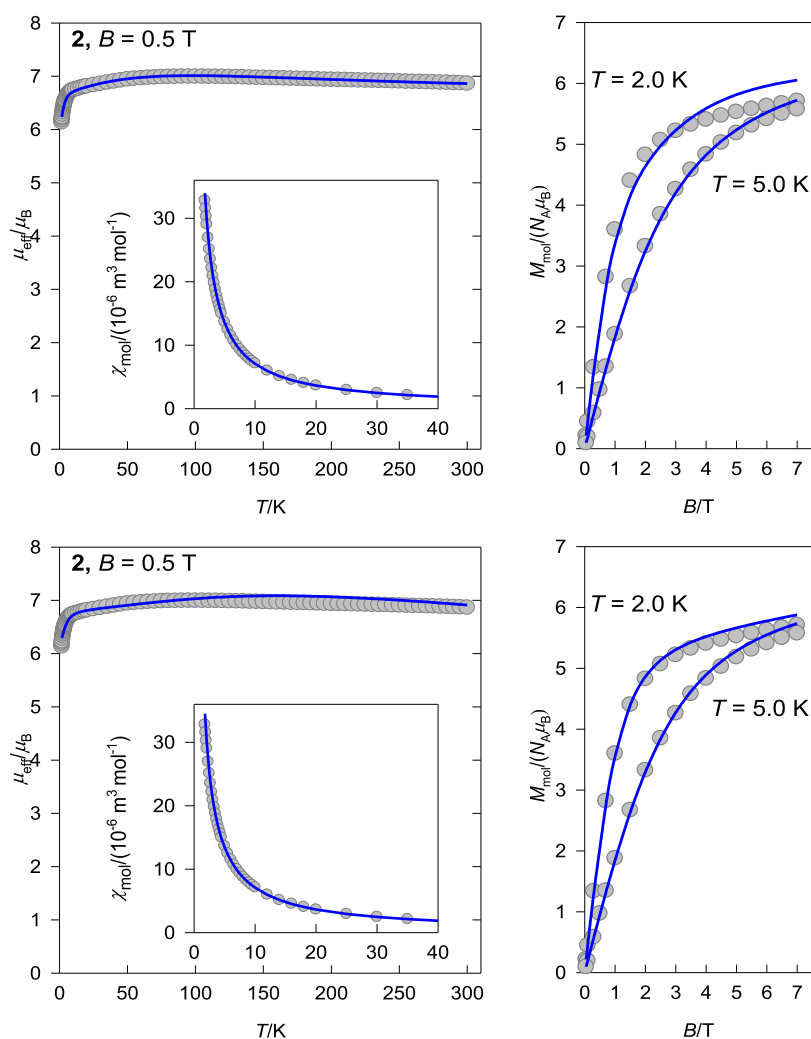


Figure 12. DC magnetic data for 2: top—fitted by the Griffith-Figgis model; bottom—using SH (see Supporting Information).

cm^{-1} , $D_{\text{Td}}/hc = -3.1 \text{ cm}^{-1}$, and $g_{\text{Td}} = 2.63$; the discrepancy factor for susceptibility is $R(\chi) = 0.017$ and for magnetization is $R(M) = 0.038$. For details, see Supporting Information.

AC Susceptibility Data. A scan of the AC susceptibility at the fixed temperature $T = 2.0 \text{ K}$ is displayed in Figure 13 as a function of the external DC field for a set of trial frequencies of the AC field.

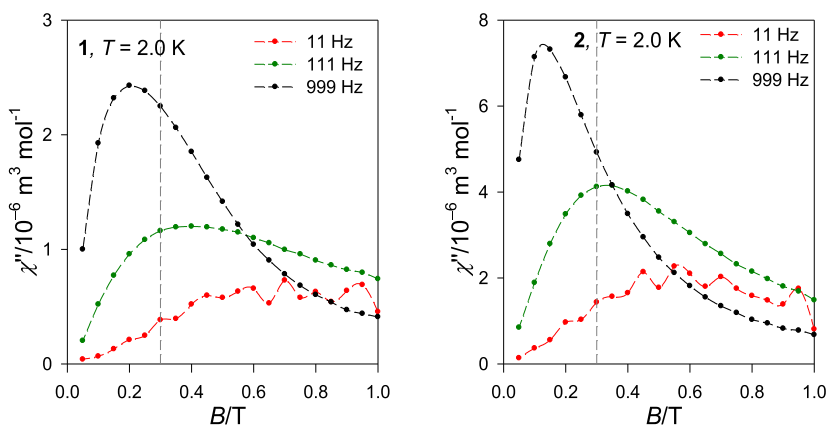


Figure 13. Field dependence of the out-of-phase susceptibility for **1** and **2** at $T = 2.0$ K for a set of trial frequencies. The lines are eye guides. A vertical bar indicates the field selected for subsequent studies: the field at which the out-of-phase susceptibility is maximum for the frequency $f = 111$ Hz.

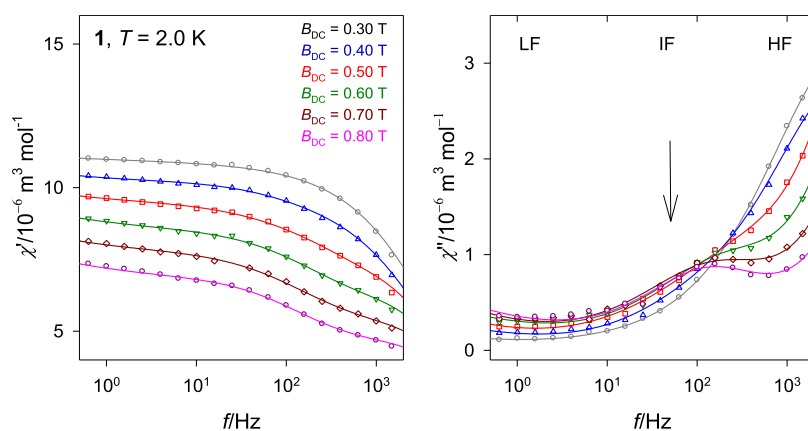


Figure 14. Frequency dependence of AC susceptibility for **1** at $T = 2.0$ K and various B_{DC} . Solid lines—fitted with the three-set Debye model.

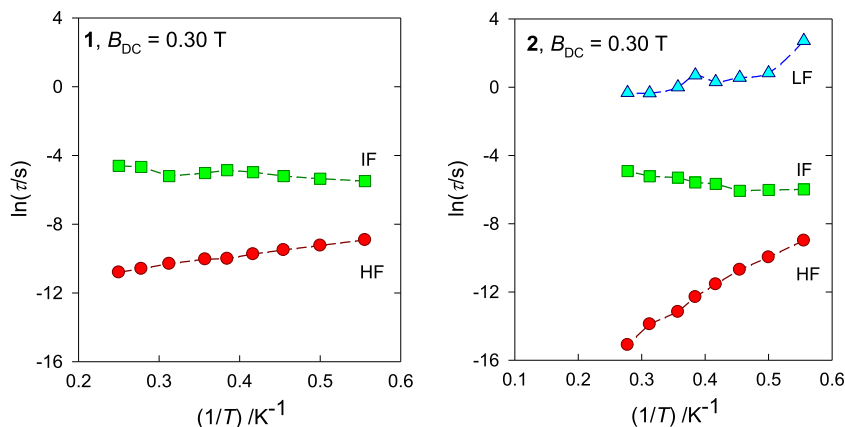


Figure 15. Arrhenius-like plot for **1** and **2**.

The out-of-phase susceptibility χ'' is zero at the zero field so that these complexes are not natural single-ion magnets. With an increasing DC magnetic field, however, the out-of-phase susceptibility rises until a maximum (different for different frequencies) and then falls down. At fields $B_{DC} \sim 0.1$ – 0.2 T, the response culminates at $f \sim 1000$ Hz; at the higher field, the response culminates at lower frequencies of $f \sim 111$ Hz.

A more detailed mapping of the frequency-field dependence at $T = 2.0$ K for **1** is shown in Figure 14. The situation is very complex since three relaxation modes are seen: low-frequency

(LF), intermediate-frequency (IF), and high-frequency (HF). The data fitting is risky since the experimental low-frequency and the high-frequency data $\chi''(f, B; [T])$ do not pass through a maximum. Consequently, the standard deviations of free parameters could be high.

The temperature and frequency dependences of the AC susceptibility components are displayed in Figures S15–S17, along with tables of fitted parameters (Tables S10–S12). The fitted values of the LF, IF, and HF relaxation times enter the Arrhenius-like plot that is depicted in Figure 15.

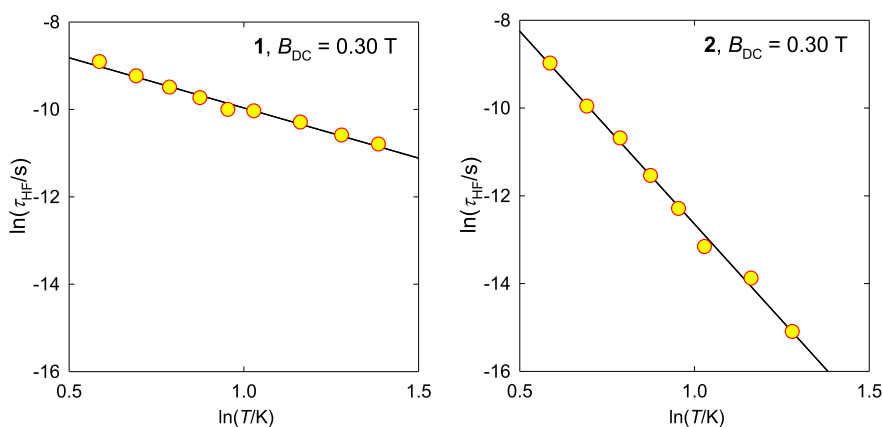


Figure 16. Analysis of the high-frequency relaxation time for **1** and **2**. Straight-line parameters $\ln \tau = b_0 + b_1 \cdot \ln T$: $b_0 = -7.67$ and $b_1 = -2.29$ for **1** ($r^2 = 0.986$); $b_0 = -3.85$ and $b_1 = -8.78$ for **2** ($r^2 = 0.996$).

It can be concluded that the HF relaxation mode follows an expected trend: with increasing temperature, the τ_{HF} decreases. These data are analyzed in Figure 16, where $\ln \tau_{\text{HF}}$ vs $\ln T$ is plotted.

The dependence follows a straight line as expected for the Raman, phonon bottleneck (PB), and direct relaxation processes: $1/\tau = CT^n$. For the Raman process, $n \sim 5-9$; for the PB-like process, $n \sim 2$; and for the direct one, $n \sim 1$, which are typical. The linear fit gave $n = 2.3$ for **1**, which is close to the expectations for the PB-like process. For **2**, $n = 8.8$ favors the Raman relaxation process. The high-frequency relaxation time at $T = 2.0$ K and $B_{\text{DC}} = 0.30$ T is $\tau(\text{HF}) = 96$ (47) μs for **1** (**2**).

Magnetostructural Correlations. To discuss the relationship between the geometry of the coordination polyhedron and the magnetic anisotropy, we start with pentacoordinated complex **1**. The $\{\text{CoN}_3\text{Cl}_2\}$ chromophore geometry most closely resembles TBV (D_{3h}), with the angular structural index parameter $\tau = 0.48$. In such a case, the ground electronic term, 4A_2 , is the orbitally non-degenerate. Therefore, the SH formalism is applicable. In line with the theory described by Nemeč²³ et al.,³¹ this rather high value of τ expects that D should be positive (crossing point at $\tau \approx 0.3$) and much above 40 cm^{-1} . The experimentally determined D values of 47.6 cm^{-1} (magnetic data) and 48 cm^{-1} (HF EPR, FIRMS), together with theoretical calculations of 48.8 cm^{-1} , fully confirm this hypothesis. A similar trend is also shown in the pentacoordinate complexes present in Table S1, Supporting Information, thus indicating the huge potential of such molecular species for achieving systems with large axial magnetic anisotropy.

The hexacoordinate Co(II) complexes are well-known to possess a ${}^4T_{1g}$ ground state in ideal Oh symmetry, which, however, is influenced by the Jahn–Teller effect, leading to geometrical distortions. The metal–ligand distances in the hexacoordinate unit of complex **2** indicate that the chromophore $\{\text{CoN}_4\text{N}_2\}$ is close to the compressed tetragonal bipyramid, for which the SH formalism is appropriate (based exclusively upon the geometric criteria). However, there are important angular distortions due to the rigidity of the ligand, measured by the angle N–Co–N = 150°. *Ab initio* calculations show the positions of the multielectron terms at 4E_g (a): $D_0 = 0$ (ground), 4E_g (b): $D_1 = 413$, and 4A_1g : $D_2 = 1412$ cm^{-1} , so there is no doubt that the ground state is an orbitally degenerate 4E_g term slightly split by the asymmetry of the coordination sphere. In such a case, the SH formalism is

inappropriate, and experimental magnetic data were treated by a Figgis–Griffith Hamiltonian model. This observation has important implications for the design of ligand systems and for isolating SIMs with targeted properties.

The tetracoordinate $[\text{Co}(\text{NCS})_4]^{2-}$ unit in complex **2** is homoleptic, which makes it difficult to calculate the δ structural parameter. Because all the pseudohalide ions are almost linear, the symmetry of the cobalt(II) ion is close to T_d , for which $D = 0$. *Ab initio* calculations resulted in a small D value of -3.7 cm^{-1} , which corresponds to the value examined from magnetic data -3.1 cm^{-1} and HF EPR/FIRMS spectra -5.65 cm^{-1} . Other examples of homoleptic tetrahedral complexes of Co(II) together with correlation with D are presented in Table S2, Supporting Information.

CONCLUSIONS

In summary, the effect of N-donor ligands and different counteranions in starting Co(II) salts leading to increased magnetic anisotropy was investigated. Mono- and binuclear Co(II) complexes with markedly distorted geometry and with different topologies have been synthesized and structurally characterized. The strong binding ability of the thiocyanate anion does not lead to the formation of the cationic complex but to a binuclear compound $[\text{Co}(\text{mpyr-dtpy})_2][\text{Co}(\text{NCS})_4]$ (**2**), which consists of strongly distorted octahedral and tetrahedral Co(II) centers. The combination of dc magnetic, FIRMS, and HFEPR measurements along with theoretical calculations unambiguously shows large magnetic anisotropy measured by the zfs parameter $D = +47.6$ for **1** and $D = -3.1$ cm^{-1} for the tetrahedral unit in **2**. For the hexacoordinate Co(II) unit in **2** with the geometry of an elongated tetragonal bipyramid, the SH formalism is invalid and the D -parameter is undefined. In such cases, the temperature evolution of the magnetic susceptibility and the field dependence of the magnetization have been fitted simultaneously by employing the Griffith–Figgis model Hamiltonian working in the space of 12 spin–orbit kets. This is the principal difference from the SH formalism that cannot be applied to the degenerate and/or quasi-degenerate ground electronic terms. This model allows us to determine a large negative value of Δ_{ax} , which is a *raison d’être* of the magnetic anisotropy of the easy-axis type. Both complexes under study display a field-supported SMR with three relaxation channels.

■ ASSOCIATED CONTENT

SI Supporting Information

The Supporting Information is available free of charge at <https://pubs.acs.org/doi/10.1021/acs.inorgchem.3c03405>.

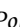
ESI-MS, FT-IR and reflectance spectra, bond lengths and angles, weak hydrogen bonds, aromatic rings interactions, structural analysis details, XPRD, and detailed magnetic data (PDF)

Accession Codes

CCDC 2260567–2260569 contain the supplementary crystallographic data for this paper. These data can be obtained free of charge via www.ccdc.cam.ac.uk/data_request/cif, or by emailing data_request@ccdc.cam.ac.uk, or by contacting The Cambridge Crystallographic Data Centre, 12 Union Road, Cambridge CB2 1EZ, UK; fax: +44 1223 336033.

■ AUTHOR INFORMATION

Corresponding Authors

Barbara Machura – Institute of Chemistry, Faculty of Science and Technology, University of Silesia, Katowice 40-006, Poland; Email: barbara.machura@us.eu.pl
Alina Bięńko – Faculty of Chemistry, Wrocław 50-383, Poland;  orcid.org/0000-0002-2714-3197; Email: alina.bienko@uwr.edu.pl

Authors

Katarzyna Choroba – Institute of Chemistry, Faculty of Science and Technology, University of Silesia, Katowice 40-006, Poland;  orcid.org/0000-0003-0168-5753
Joanna Palion-Gazda – Institute of Chemistry, Faculty of Science and Technology, University of Silesia, Katowice 40-006, Poland;  orcid.org/0000-0002-8239-6453
Daria Wojtala – Faculty of Chemistry, Wrocław 50-383, Poland
Dariusz Bięńko – Faculty of Chemistry, Wrocław University of Science Technology, Wrocław 50-370, Poland
Cyril Rajnák – Faculty of Health Science and Faculty of Natural Sciences, University of SS Cyril and Methodius, Trnava SK-917 01, Slovakia;  orcid.org/0000-0003-2173-6220
Roman Boča – Institute of Chemistry, Faculty of Science and Technology, University of Silesia, Katowice 40-006, Poland;  orcid.org/0000-0003-0222-9434
Andrew Ozarowski – National High Magnetic Field Laboratory, Florida State University, Tallahassee, Florida 32310, United States;  orcid.org/0000-0001-6225-9796
Mykhaylo Ozerov – National High Magnetic Field Laboratory, Florida State University, Tallahassee, Florida 32310, United States;  orcid.org/0000-0002-5470-1158

Complete contact information is available at: <https://pubs.acs.org/doi/10.1021/acs.inorgchem.3c03405>

Author Contributions

The manuscript was written through contributions of all authors. All authors have given approval to the final version of the manuscript.

Notes

The authors declare no competing financial interest.

■ ACKNOWLEDGMENTS

The magnetic measurements and analysis were supported by the University of Wrocław program IDUB (BPIDUB.4610.17.2021.KP.B.) (A.B.). Slovak grant agencies (APVV 19-0087, VEGA 1/0191/22, and VEGA 1/0086/21) are acknowledged for the financial support. The National High Magnetic Field Laboratory is supported by the National Science Foundation Cooperative Agreement no. DMR-7631644779 and DMR-2128556 (A.O.; M.O.) and the State of Florida. The research activities are cofinanced by the funds granted under the Research Excellence Initiative of the University of Silesia in Katowice.

■ ABBREVIATIONS

SIMs, single-ion magnets; SMMs, single-molecule magnets; zfs, zero-field splitting; U_{eff} , effective energy barrier; Δ_{ax} , term splitting; SH, spin-Hamiltonian; HF, high-frequency; LF, low-frequency; IF, intermediate-frequency; dppy, 2,6-di(thiazol-2-yl)pyridine; mpyr-dtpy, 4-(N-methyl-pyrrol-2-yl)-2,6-di(thiazol-2-yl)pyridine; terpy, 2,2':6',2''-terpyridine; TBPY, trigonal bipyramid; OC, octahedron; SPY, square pyramid; XRPD, powder X-ray diffraction; CSHM, continuous shape measurement; HFEP, high-field EPR; FIRMS, far-infrared magnetic spectroscopy; CASSCF, complete active space self-consistent field; SOMF, spin-orbit mean-field

■ REFERENCES

- (1) Craig, G. A.; Murrie, M. 3d Single-Ion Magnets. *Chem. Soc. Rev.* **2015**, *44*, 2135–2147.
- (2) Gómez-Coca, S.; Aravena, D.; Morales, R.; Ruiz, E. Large Magnetic Anisotropy in Mononuclear Metal Complexes. *Coord. Chem. Rev.* **2015**, *289–290*, 379–392.
- (3) Frost, J. M.; Harriman, K. L. M.; Murugesu, M. The Rise of 3-d Single-Ion Magnets in Molecular Magnetism: Towards Materials from Molecules? *Chem. Sci.* **2016**, *7*, 2470–2491.
- (4) Zadrozny, J. M.; Long, J. R. Slow Magnetic Relaxation at Zero Field in the Tetrahedral Complex $[\text{Co}(\text{SPH})_4]^{2-}$. *J. Am. Chem. Soc.* **2011**, *133*, 20732–20734.
- (5) Zadrozny, J. M.; Telser, J.; Long, J. R. Slow Magnetic Relaxation in the Tetrahedral Cobalt(II) Complexes $[\text{Co}(\text{EPH})_4]^{2-}$ (EO, S, Se). *Polyhedron* **2013**, *64*, 209–217.
- (6) Boča, R.; Miklovič, J.; Titiš, J. Simple Mononuclear Cobalt(II) Complex: A Single-Molecule Magnet Showing Two Slow Relaxation Processes. *Inorg. Chem.* **2014**, *53*, 2367–2369.
- (7) Packová, A.; Miklovič, J.; Boča, R. Manifold Relaxation Processes in a Mononuclear Co(II) Single-Molecule Magnet. *Polyhedron* **2015**, *102*, 88–93.
- (8) Sottini, S.; Poneti, G.; Ciattini, S.; Levesanos, N.; Ferentinos, E.; Krzystek, J.; Sorace, L.; Kyritsis, P. Magnetic Anisotropy of Tetrahedral Co^{II} Single-Ion Magnets: Solid-State Effects. *Inorg. Chem.* **2016**, *55*, 9537–9548.
- (9) Świtlicka, A.; Machura, B.; Penkala, M.; Bięńko, A.; Bięńko, D. C.; Titiš, J.; Rajnák, C.; Boča, R.; Ozarowski, A.; Ozerov, M. Slow Magnetic Relaxation in Cobalt(II) Field-Induced Single-Ion Magnets with Positive Large Anisotropy. *Inorg. Chem.* **2018**, *57*, 12740–12755.
- (10) Świtlicka, A.; Machura, B.; Penkala, M.; Bięńko, A.; Bięńko, D. C.; Titiš, J.; Rajnák, C.; Boča, R.; Ozarowski, A. Slow Magnetic Relaxation in Hexacoordinated Cobalt(II) Field-Induced Single-Ion Magnets. *Inorg. Chem. Front.* **2020**, *7*, 2637–2650.
- (11) Świtlicka, A.; Machura, B.; Bięńko, A.; Koziel, S.; Bięńko, D. C.; Rajnák, C.; Boča, R.; Ozarowski, A.; Ozerov, M. Non-traditional Thermal Behavior of Co(II) Coordination Networks Showing Slow Magnetic Relaxation. *Inorg. Chem. Front.* **2021**, *8*, 4356–4366.
- (12) Tripathi, S.; Dey, A.; Shanmugam, M.; Narayanan, R. S.; Chandrasekhar, V. Cobalt(II) Complexes as Single-Ion Magnets. *Top. Organomet. Chem.* **2018**, *64*, 35–75.

- (13) Juráková, J.; Šalitroš, I. Co(II) Single-Ion Magnets: Synthesis, Structure, and Magnetic Properties. *Monatsh. Chem.* **2022**, *153*, 1001–1036.
- (14) Kumar Sahu, P.; Kharel, R.; Shome, S.; Goswami, S.; Konar, S. Understanding the Unceasing Evolution of Co(II) Based Single-Ion Magnets. *Coord. Chem. Rev.* **2023**, *475*, 214871.
- (15) Pini, M. G.; Rettori, A.; Bogani, L.; Lascialfari, A.; Mariani, M.; Caneschi, A.; Sessoli, R. Finite-Size Effects on the Dynamic Susceptibility of CoPhOMe Single-Chain Molecular Magnets in Presence of a Static Magnetic Field. *Phys. Rev. B: Condens. Matter Mater. Phys.* **2011**, *84*, 094444.
- (16) Murrie, M. Cobalt(II) Single-Molecule Magnets. *Chem. Soc. Rev.* **2010**, *39*, 1986–1995.
- (17) Kramers, H. A. Théorie Générale de la Rotation Paramagnétique dans les Cristaux. *Proc. Rochester Acad. Sci.* **1930**, *33*, 959–972.
- (18) Vaidya, S.; Tewary, S.; Singh, S. K.; Langley, S. K.; Murray, K. S.; Lan, Y.; Wernsdorfer, W.; Rajaraman, G.; Shanmugam, M. What Controls the Sign and Magnitude of Magnetic Anisotropy in Tetrahedral Cobalt(II) Single-Ion Magnets? *Inorg. Chem.* **2016**, *55*, 9564–9578.
- (19) Gomez-Coca, S.; Urtizberea, A.; Cremades, E.; Alonso, P. J.; Camon, A.; Ruiz, E.; Luis, F. Origin of Slow Magnetic Relaxation in Kramers Ions with Non-uniaxial Anisotropy. *Nat. Commun.* **2014**, *5* (1), 4300.
- (20) Chen, Z.-W.; Yin, L.; Mi, X. N.; Wang, S. N.; Cao, F.; Wang, Z. X.; Li, Y. W.; Lu, J.; Dou, J. M. Field-Induced Slow Magnetic Relaxation of two 1-D Compounds Containing Six-coordinated Cobalt(ii) Ions: Influence of the Coordination Geometry. *Inorg. Chem. Front.* **2018**, *5*, 2314–2320.
- (21) Rechkemmer, Y.; Breitgoff, F. D.; Van der Meer, M.; Atanasov, M.; Hakl, M.; Orlita, M.; Neugebauer, P.; Neese, F.; Sarkar, B.; Van Slageren, J. A four-coordinate cobalt(II) single-ion magnet with coercivity and a very high energy barrier. *Nat. Commun.* **2016**, *7*, 10467.
- (22) Titiš, J.; Miklovič, J.; Boča, R. Magnetostructural Study of Tetracoordinate Cobalt(II) Complexes. *Inorg. Chem. Commun.* **2013**, *35*, 72–75.
- (23) Nemeč, I.; Herchel, R.; Kern, M.; Neugebauer, P.; Van Slageren, J.; Trávníček, Z. Magnetic Anisotropy and Field-Induced Slow Relaxation of Magnetization in Tetracoordinate Co^{II} Compound [Co(CH₃-im)₂Cl₂]. *Materials* **2017**, *10*, 249.
- (24) Saber, M. R.; Dunbar, K. R. Ligands Effects on the Magnetic Anisotropy of Tetrahedral Cobalt Complexes. *Chem. Commun.* **2014**, *50*, 12266–12269.
- (25) Buvaylo, E. A.; Kokozay, V. N.; Vassilyeva, O.; Skelton, B. W.; Ozarowski, A.; Titiš, J.; Vranovičová, B.; Boča, R. Field-Assisted Slow Magnetic Relaxation in a Six-Coordinate Co(II)-Co(III) Complex with Large Negative Anisotropy. *Inorg. Chem.* **2017**, *56*, 6999–7009.
- (26) Valigura, D. C.; Rajnák, C.; Moncol, J.; Titiš, J.; Boča, R. A Mononuclear Co(II) Complex Formed from Pyridinedimethanol with Manifold Slow Relaxation Channels. *Dalton Trans.* **2017**, *46*, 10950–10956.
- (27) Massoud, S. S.; Fischer, R. C.; Mautner, F. A.; Parfait, M. M.; Herchel, R.; Trávníček, Z. Pentacoordinate Cobalt(II) Complexes with Neutral Tripodal N-Donor ligands: Zero-field Splitting for a Distorted Trigonal Bipyramidal Geometry. *Inorg. Chim. Acta* **2018**, *471*, 630–639.
- (28) Cui, H.-H.; Xu, H.; Zhang, M.; Luo, S.; Tong, W.; Wang, M.; Sun, T.; Chen, L.; Tang, Y. Magnetic Anisotropy from Easy-Plane to Easy-Axial in Square Pyramidal Cobalt(II) Single-Ion Magnets. *Cryst. Growth Des.* **2022**, *22*, 2742–2748.
- (29) Shao, D.; Deng, L.-D.; Shi, L.; Wu, D.-Q.; Wei, X.-Q.; Yang, S.-R.; Wang, X.-Y. Slow Magnetic Relaxation and Spin-Crossover Behavior in a Bicomponent Ion-Pair Cobalt(II) Complex. *Eur. J. Inorg. Chem.* **2017**, *2017*, 3862–3867.
- (30) Rajnák, C.; Varga, F.; Titiš, J.; Moncol, J.; Boča, R. Octahedral-Tetrahedral Systems [Co(dppm^o,^o)₃]²⁺[CoX₄]²⁻ Showing Slow Magnetic Relaxation with Two Relaxation Modes. *Inorg. Chem.* **2018**, *57*, 4352–4358.
- (31) Ozumerzifon, T. J.; Bhowmick, I.; Spaller, W. C.; Rappé, A. K.; Shores, M. P. Toward Steric Control of Guest Binding Modality: A Cationic Co(II) Complex Exhibiting Cation Binding and Zero-Field Relaxation. *Chem. Commun.* **2017**, *53*, 4211–4214.
- (32) Ghosh, S.; Kamilya, S.; Das, M.; Mehta, S.; Boulon, M.-E.; Nemeč, I.; Rouzières, M.; Herchel, R.; Mondal, A. Effect of Coordination Geometry on Magnetic Properties in a Series of Cobalt(II) Complexes and Structural Transformation in Mother Liquor. *Inorg. Chem.* **2020**, *59*, 7067–7081.
- (33) Massoud, S. S.; Dubin, M.; Guilbeau, A. E.; Spell, M.; Vicente, R.; Wilfling, P.; Fischer, R. C.; Mautner, F. A. Azido- and Thiocyanato-Cobalt(II) Complexes Based Pyrazole Ligands. *Polyhedron* **2014**, *78*, 135–140.
- (34) Palion-Gazda, J.; Machura, B.; Kruszynski, R.; Granča, T.; Moliner, N.; Lloret, F.; Julve, M. Spin Crossover in Double Salts Containing Six- and Four-Coordinate Cobalt(II) Ions. *Inorg. Chem.* **2017**, *56*, 6281–6296.
- (35) Zhang, Y.; Harriman, K. L. M.; Brunet, G.; Pialat, A.; Gابدullin, B.; Murugesu, M. Reversible Redox, Spin Crossover, and Superexchange Coupling in 3d Transition-Metal Complexes of Bis-Azanyl Analogues of 2,2':6',6''-Terpyridine. *Eur. J. Inorg. Chem.* **2018**, *2018*, 1212–1223.
- (36) Boča, M.; Boča, R.; Kickelbick, G.; Linert, W.; Svoboda, I.; Fuess, H. Novel Complexes of 2,6-Bis(benzthiazol-2-yl)pyridine. *Inorg. Chim. Acta* **2002**, *338*, 36–50.
- (37) Nobbs, J. D.; Tomov, A. K.; Cariou, R.; Gibson, V. C.; White, A. J. P.; Britovsek, G. J. P. Thio-Pybox and Thio-Phebox Complexes of Chromium, Iron, Cobalt and Nickel and their Application in Ethylene and Butadienepolymerisation catalysis. *Dalton Trans.* **2012**, *41*, 5949–5964.
- (38) Li, G.-Y.; Du, K.-J.; Wang, J.-Q.; Liang, J.-W.; Kou, J.-F.; Hou, X.-J.; Ji, L.-N.; Chao, H. Synthesis, Crystal Structure, DNA Interaction and Anticancer Activity of Tridentate Copper(II) Complexes. *J. Inorg. Biochem.* **2013**, *119*, 43–53.
- (39) Li, L.; Du, K.; Wang, Y.; Jia, H.; Hou, X.; Chao, H.; Ji, L. Self-activating Nuclease and Anticancer Activities of Copper(II) Complexes with Aryl-modified 2,6-Di(thiazol-2-yl)pyridine. *Dalton Trans.* **2013**, *42*, 11576–11588.
- (40) Czerwińska, K.; Machura, B.; Kula, S.; Krompiec, S.; Erfurt, K.; Roma-Rodrigues, C.; Fernandes, A. R.; Shul'pina, L. S.; Ikonnikov, N. S.; Shul'pin, G. B. Copper(II) Complexes of Functionalized 2,2':6',6''-Terpyridines and 2,6-Di(thiazol-2-yl)pyridine: Structure, Spectroscopy, Cytotoxicity and Catalytic Activity. *Dalton Trans.* **2017**, *46*, 9591–9604.
- (41) Nguyen, M. T.; Jones, R. A.; Holliday, B. J. Incorporation of Spin-Crossover Cobalt(II) Complexes into Conducting Metallopolymers: Towards Redox-controlled Spin Change. *Polymer* **2021**, *222*, 123658.
- (42) Macrae, C. F.; Bruno, I. J.; Chisholm, J. A.; Edgington, P. R.; McCabe, P.; Pidcock, E.; Rodriguez-Monge, L.; Taylor, R.; van de Streek, J.; Wood, P. A. Mercury CSD 2.0—New Features for the Visualization and Investigation of Crystal Structures. *J. Appl. Crystallogr.* **2008**, *41*, 466–470.
- (43) *CrysAlisPRO*; Oxford Diffraction; Agilent Technologies UK Ltd: Yarnton, England, 2014.
- (44) Sheldrick, G. M. Phase Annealing in SHELX-90: Direct Methods for Larger Structures. *Acta Crystallogr.* **1990**, *46*, 467–473.
- (45) Sheldrick, G. M. A Short History of SHELX. *Acta Crystallogr., Sect. A: Cryst. Phys., Diff., Theor. Gen. Crystallogr.* **2008**, *64*, 112–122.
- (46) Sheldrick, G. M. SHELXT—Integrated Space-Group and Crystal-Structure Determination. *Acta Crystallogr., Sect. A: Cryst. Phys., Diff., Theor. Gen. Crystallogr.* **2015**, *71*, 3–8.
- (47) Hassan, A.; Pardi, L.; Krzystek, J.; Sienkiewicz, A.; Goy, P.; Rohrer, M.; Brunel, L.-C. Ultrawide Band Multifrequency High-Field EMR Technique: A Methodology for Increasing Spectroscopic Information. *J. Magn. Reson.* **2000**, *142*, 300–312.
- (48) The program can be accessed at <https://osf.io/z72tg/>.

- (49) Boča, R. *Program MIF&FIT*; University of SS Cyril and Methodius: Trnava, 2022.
- (50) Neese, F. The ORCA Program System. *WIREs Comput. Mol. Sci.* **2012**, *2*, 73–78.
- (51) Neese, F. *ORCA—An Ab Initio, Density Functional and Semiempirical Program Package*. version 5.0.2, 2022.
- (52) Neese, F.; Wennmohs, F.; Becker, U.; Riplinger, C. The ORCA Quantum Chemistry Program Package. *J. Chem. Phys.* **2020**, *152*, 224108.
- (53) Maurice, R.; Bastardis, R.; Graaf, C. d.; Suaud, N.; Mallah, T.; Guihéry, N. Universal Theoretical Approach to Extract Anisotropic Spin Hamiltonians. *J. Chem. Theory Comput.* **2009**, *5*, 2977–2984.
- (54) Habib, F.; Luca, O. R.; Vieru, V.; Shiddiq, M.; Korobkov, I.; Gorelsky, S. I.; Takase, M. K.; Chibotaru, L. F.; Hill, S.; Crabtree, R. H.; Murugesu, M. Influence of the Ligand Field on Slow Magnetization Relaxation versus Spin Crossover in Mononuclear Cobalt Complexes. *Angew. Chem., Int. Ed.* **2013**, *52*, 11290–11293.
- (55) Zhang, G.; Tan, J.; Zhang, Y. Z.; Ta, C.; Sanchez, S.; Cheng, S. Y.; Golen, J. A.; Rheingold, A. L. Syntheses, Structures and Cytotoxicity of Cobalt(II) Complexes with 4'-chloro-2,2':6',2''-terpyridine. *Inorg. Chim. Acta* **2015**, *435*, 147–152.
- (56) Constable, E. C.; Harris, K.; Housecroft, C. E.; Neuburger, M.; Zampese, J. A. Environmental Control of Solution Speciation in Cobalt(II) 2,2':6',2''-Terpyridine Complexes: Anion and Solvent Dependence. *Dalton Trans.* **2011**, *40*, 11441–11450.
- (57) Bray, D. J.; Clegg, J. K.; Jolliffe, K. A.; Lindoy, L. F. Cobalt(II), Iron(II), Zinc(II) and Palladium(II) Complexes of di-topic 4'-{4-[bis(2-pyridyl)aminomethyl]phenyl}-2,2':6',2''-terpyridine. Synthetic and X-ray Structural Studies. *CrystEngComm* **2014**, *16*, 6476–6482.
- (58) Wałęsa-Chorab, M.; Gorczyński, A.; Kubicki, M.; Korabik, M.; Patroniak, V. Mono-Di- and Trinuclear Complexes of Bis-(terpyridine) Ligand: Synthesis, Crystal Structures and Magnetic Properties. *Polyhedron* **2013**, *54*, 260–271.
- (59) Addison, A. W.; Rao, T. N.; Reedijk, J.; van Rijn, J.; Verschoor, G. C. Synthesis, Structure, and Spectroscopic Properties of Copper(II) Compounds Containing Nitrogen-Sulphur Donor Ligands; the Crystal and Molecular Structure of aqua[1,7-bis(N-methylbenzimidazol-2'-yl)-2,6-dithiaheptane]copper(II) perchlorate. *J. Chem. Soc., Dalton Trans.* **1984**, 1349–1356.
- (60) Llunell, M.; Casanova, D.; Cirera, J.; Alemany, P.; Alvarez, S. *SHAPE*. version 2.0; Universitat de Barcelona, 2010.
- (61) Choroba, K.; Machura, B.; Kula, S.; Raposo, L. R.; Fernandes, A. R.; Kruszynski, R.; Erfurt, K.; Shul'pina, L. S.; Kozlov, Y. N.; Shul'pin, G. B. Copper(II) complexes with 2,2':6',2''-Terpyridine, 2,6-Di(thiazol-2-yl)pyridine and 2,6-Di(pyrazin-2-yl)pyridine Substituted with Quinolines. Synthesis, Structure, Antiproliferative Activity, and Catalytic Activity in the Oxidation of Alkanes and Alcohols with Peroxides. *Dalton Trans.* **2019**, *48*, 12656–12673.
- (62) Cirera, J.; Ruiz, E.; Alvarez, S. Continuous Shape Measures as a Stereochemical Tool in Organometallic Chemistry. *Organometallics* **2005**, *24*, 1556–1562.
- (63) Casanova, D.; Llunell, M.; Alemany, P.; Alvarez, S. The Rich Stereochemistry of Eight-Vertex Polyhedra: A Continuous Shape Measures Study. *Chem.—Eur. J.* **2005**, *11*, 1479–1494.
- (64) Okuniewski, A.; Rosiak, D.; Chojnacki, J.; Becker, B. Coordination Polymers and Molecular Structures Among Complexes of Mercury(II) Halides with Selected 1-Benzoylthioureas. *Polyhedron* **2015**, *90*, 47–57.
- (65) Macrae, C. F.; Edgington, P. R.; McCabe, P.; Pidcock, E.; Shields, G. P.; Taylor, R.; Towler, M.; van de Streek, J. Mercury: Visualization and Analysis of Crystal Structures. *J. Appl. Crystallogr.* **2006**, *39*, 453–457.
- (66) Boča, R.; Rajnák, C.; Titiš, J. Possible Violation of the Spin-Hamiltonian Concept in Interpreting the Zero-Field Splitting. *J. Phys. Chem. A* **2023**, *127*, 3256–3264.
- (67) Boča, R.; Rajnák, C.; Titiš, J. Zero-Field Splitting in Hexacoordinate Co(II) complexes. *Magnetochemistry* **2023**, *9*, 100.

Recommended by ACS

Spectroscopic and Theoretical Investigation of High-Spin Square-Planar and Trigonal Fe(II) Complexes Supported by Fluorinated Alkoxides

Léa A. Toubiana, Sebastian A. Stoian, *et al.*

JANUARY 23, 2024

INORGANIC CHEMISTRY

READ 

Enhancing Spin-Transport Characteristics, Spin-Filtering Efficiency, and Negative Differential Resistance in Exchange-Coupled Dinuclear Co(II) Complexes for Molecular Spint...

Rupesh Kumar Tiwari, Gopalan Rajaraman, *et al.*

DECEMBER 19, 2023

INORGANIC CHEMISTRY

READ 

Solvatotuning of the Field-Induced Slow Magnetic Relaxation through a Single-Crystal-to-Single-Crystal Transformation in Pentanuclear Gadolinium(III)-Nickel(I...

Nadia El Alouani-Dahmouni, Joan Cano, *et al.*

JUNE 27, 2023

CRYSTAL GROWTH & DESIGN

READ 

Semiempirical Magnetostructural Correlation for High-Nuclearity Mn^{III}-Oxo Complexes: Accommodation of Different Relative Jahn–Teller Axis Orientations

Kenneth Hong Kit Lee and George Christou

NOVEMBER 03, 2023

INORGANIC CHEMISTRY

READ 